Master's thesis

NTNU
Norwegian University of Science and Technology
Faculty of Information Technology and Electrical Engineering
Department of Electric Power Engineering

Jørgen Hagset Stavnesli

Control Strategies of a Converter-Fed Synchronous Machine for Variable Speed Hydropower

Master's thesis in Energy and Environmental Engineering

Supervisor: Jonas K. Nøland

June 2020

NTNU
Norwegian University of Science and Technology

Jørgen Hagset Stavnesli

Control Strategies of a Converter-Fed Synchronous Machine for Variable Speed Hydropower

Master's thesis in Energy and Environmental Engineering
Supervisor: Jonas K. Nøland
June 2020

Norwegian University of Science and Technology
Faculty of Information Technology and Electrical Engineering
Department of Electric Power Engineering

NTNU
Norwegian University of
Science and Technology

Preface

This Master's thesis serves as the conclusion to my five-year Master's degree in Energy and Environmental Engineering at NTNU and is a continuation of work done by former NTNU Master's students performing system studies on variable speed hydropower plants. Variable speed operation of hydropower plants is one of the main research areas in HydroCen, an NTNU affiliated research centre for environmental-friendly energy research (FME). The thesis differs from the previous theses, who focused primarily on system modelling and grid integration, by taking a more in-depth focus on the excitation system of the converter-fed synchronous machine.

The topic and scope of this thesis posed an interesting challenge for me, as I both had to use and expand my knowledge about the modelling and control of synchronous machines, frequency converters and hydraulic systems. With such a large and complex system, a lot of work was done to read about the operation and behaviour of a variable speed hydropower plant. Furthermore, the modelling of the system presented in this thesis took the greater part of the work time during this semester. Therefore, much of the work that has done may not be visible in this thesis.

I would like to thank my supervisor, Jonas Nøland, and co-supervisor Gilbert Bergna-Diaz, for helping me out and providing me with guidance during the course of this thesis.

Summary

Pumped-storage hydropower plants are seen as one of the best solutions for efficient, large-scale energy storage, and have for a long time been used for balancing the supply-demand gap on an intraday basis. However, as the share of intermittent renewable energy sources is growing, there will be a need for more controllable power plants in the grid that are able to better compensate for fluctuations in the generation of power. The progress in power electronics has enabled synchronous machines to be fed by frequency converters with a rating of up to 100 MVA to employed for pumped-storage hydropower applications. By using full-sized converters, the hydro-electric plant is decoupled from the grid, thus bringing new possibilities for control of the plant.

This thesis examines the control of a converter-fed synchronous machine for a pumped-storage plant, studying the excitation system control and various forms of power control. For this purpose, a model of an 8 kVA converter-fed synchronous machine was created in Simulink, where both pump-mode and generation-mode could be simulated. The excitation system controller was implemented with the objective of controlling Ψ_s to 1.0 pu, which had the effect of improving the torque-per-ampere ratio of the machine, while also avoiding operation of the machine in saturation. Power control of the pump load, in the form of a load-following controller and a frequency controller, illustrated the potential for improved grid support when the pumped-storage plant is allowed to operate in variable speed. In addition, inertia controllers for the kinetic energy in the rotor and the stored energy in the dc-link capacitor were implemented. The inertia controllers indicated the ability of the converter-fed synchronous machine system to quickly respond to grid disturbances, without the need to start ramping of the prime mover. For further work, the model should be updated to include a MW-scale machine and explore the possibilities of virtual synchronous machine control in generation mode.

Samandrag

Pumpekraftverk vert sett på som ei effektiv form for storskala energilagring, og har i long tid vore brukt for utjevning av forbruk og etterspørsel på dagsbasis. Framtidas kraftnett vil sjå eit auka behov for kontrollerbare kraftverk, som kan veie opp for innslag av fornybare energikilder prega av større varians i kraftproduksjon. Framsteg i kraftelektronikk har gjort det mogleg å installere frekvensomformera med ei merkeeffekt på opp mot 100 MVA til bruk for variabel turtallsdrift av pumpekraftverk. Ved å bruke ein frekvensomformar, så vert kraftverket uavhengig av nettfrekvensen, noke som gir potensiale for nye måtar å regulere drifta av kraftverket på.

Denne masteroppgava utforskar ulike kontrollaspekt ved omformer-mata synkronmaskinar, med eit fokus på magnetiseringssystemet og ulike forma for effektkontroll. Ein modell av ein omformer-mata synkronmaskin i eit pumpekraftverk vart modellert ved hjelp av simuleringsverktøyet Simulink, både for pumpe- og generator-drift. Ein flux-kontroller vart implementert for magnetiseringssystemet som gjorde at eit høgare moment-per-ampere vart oppnådd. Effektkontroll av pumpelasta, i form av ”Load following”-kontroll og frekvenskontrollert last, vart òg undersøkt og viste seg å gi kraftverket ein auka eigenskap til å støtte det eksterne nettet. Til slutt så vart to typar ”inertia”-kontrollarar implementert, og dei viste at systemet òg er i stand til å emulere treghet, noko som vart gjort ved å senke eller auke enten hastigheten eller dc-spenningen. For vidare arbeid med denne oppgaven så tilrådas det å byte ut 8 kVA maskina frå modellen med ein anna som ligger på omtrent 10-100 MW størrelse for meir realistiske simuleringar og test scenarioar. Ein anna ting vil være å sjå på ”virtual synchronous machine”-kontroll av maskina i generator-drift.

Table of Contents

List of Tables

List of Figures

Abbreviations

PSH Pumped-Storage Hydropower

TPA Torque-per-Ampere

CFSM Converter-Fed Synchronous Machine

AC Alternating Current

DC Direct Current

RPM Rounds-per-Minute

MSC Machine-Side Converter

GSC Grid-Side Converter

Subscripts

d d-axis

q q-axis

0 0-axis

s Stator quantity

D d-axis damper winding

Q q-axis damper winding

fd Field quantity

m,mech Mechanical quantity

g,gen Generator quantity

grid Grid quantity

m Magnetization

ref Reference value

e Electrical quantity

f Frequency

dc DC-link quantity

line Line voltage

rms RMS value

n Nominal value

msc Machine-side converter quantity

gsc Grid-side converter quantity

List of Symbols

Ψ Flux linkage

v, V Voltage

i, I Current

ω Angular speed

θ Angular position

n Speed in rpm

r, R Resistance

l, L Inductance

x, X Reactance

P Active power

Q Reactive power

S Apparent power

T Torque

t Time, time constant

$\cos\varphi$ Power factor

K, k Constant, Gain

Chapter 1

Introduction

To properly integrate the increasing amounts of wind and solar energy into the power grid, there is a need for large-scale energy storage systems that may balance the supply-demand gap during power fluctuations. Today, existing battery and hydrogen storage solutions are simply too expensive and small-scale, such that the only practical way of storing MW to TW amounts of energy is by using Pumped-Storage Hydropower (PSH) plants [3]. PSH plants have for some time been used to support nuclear and coal-fired plants by balancing power fluctuations on an intraday basis. However, the conventional PSH plant have limited controllability of the pump load due to being bound to operating at a constant fixed-speed. An improvement to the PSH technology is to install a full-sized frequency converter to enable variable speed operation. By being fed from a frequency converter, the synchronous machine have greater possibilities for improved control, since the frequency converter can freely regulate the voltage and frequency fed to the machine, as well the power delivered to the grid. As a consequence of the decoupling of machine and grid, several aspects of the conventional hydropower plant can be improved, including: increased hydraulic efficiency at part load, power control in pump mode, optimization of electric system and other grid-side support services such as synthetic inertia [4].

1.1 Objective and Scope of Work

The objective of this master's thesis was to explore control strategies for variable speed pumped-storage plant. Based on this objective, the following work was performed during the course of this master thesis.

1. Developed a Simulink model of variable speed pumped-storage plant.
2. Implementation of an excitation system control strategy based on optimal torque-per-ampere.
3. Examined different control strategies for utilization of the variable speed PSH plant in the power system.

1.2 Structure

Chapter 1 - Introduction: Provides the background for the thesis and gives an overview of its objectives and structure.

Chapter 2 - Variable Speed Hydropower: Introduces the concept of pumped-storage hydropower and present the motivation for variable speed operation.

Chapter 3 - System Modelling: Explains the modelling of the converter-fed synchronous machine, the prime movers and the converters.

Chapter 4 - Excitation Control of the Synchronous Machine: Examines the role of the excitation system for a converter-fed synchronous machine. Present the modelling of saturation effects, and implements a controller strategy for optimal torque-per-ampere.

Chapter 5 - Control Strategies for Variable Speed Hydropower: Examines different control strategies for a grid-connected variable speed pumped-storage plant. The scenarios focuses on load balancing, frequency support and synthetic inertia.

Chapter 6 - Results: Presents the results from the analysis of the excitation system control strategy and the control scenarios for variable speed hydropower.

Chapter 7 - Analysis: Discuss the main findings and results of the thesis, including remarks about the system modelling and its limitations, the excitation system control strategy and control scenarios for variable speed hydropower.

Chapter 8 - Conclusion: Sums up the work of this thesis in short paragraphs before providing some thoughts on shortcomings and possible further work from the author.

Chapter 2

Variable Speed Hydropower

Any machine or generator directly connected to the grid frequency must operate at a fixed-speed to abide grid regulations. For many applications, fixed-speed operation under partial loading is undesired as this often leads to reduced efficiency or increased fuel consumption. This is true for hydropower plants as well, which due to the market-oriented operation of power plants operates at part load more frequently. Attention has for some time been drawn to variable speed operation of Pumped-Storage Hydropower (PSH) plants, which will be the most relevant application of variable speed technology of large scale hydropower plants [1].

PSH plants are a practical and relatively efficient way of storing a large amount of energy, considered to have a typical round-trip efficiency between 70-85 % [5]. These plants work as both a motor and a generator, pumping water back up to the reservoir or releasing water to act as a conventional hydroelectric power plant. Conventional PSH plants have for many years been used to balance production and demand, where a typical operation regime is to work in pump mode during off-peak hours at night and in generating mode when load demand is high during the day. The ability to work as a load and a generator provides power system operators with the flexibility needed for efficiency optimization of nuclear and thermal plants [6].

A drawback of fixed-speed pump-turbines is their limited ability to adjust power in pump mode, due to being limited to operate at a constant speed. As the energy mix in many power systems is further influenced by intermittent energy sources such as wind and solar, it would be desirable to have power plants offering highly-responsive power adjusting services [1]. Fixed-speed system can solve this challenge by utilizing ternary systems, which are a pump and a turbine connected to the same shaft, thus enabling pumping and generation at the same time [5]. Other solutions use multiple pumps, such that variable pump load is achieved by starting or stopping of one or more the pumps. The disadvantages of this are that ternary systems can be quite complex with high operating and maintenance costs. In addition, multiple pump systems require increased investments and equipment,

when what could be one large pump-turbine is divided into several smaller pump-turbines.

Therefore, the main motivation for implementing variable speed operation of PSH plants is the ability to adjust power over a wide range in pump mode [5][7]. The power output of a reversible pump-turbine in this mode is dependent on the speed of the runner, and the operating head [7]. Hence, it is quite clear that by being able to operate at $\pm$ 30% of rated speed, the achieved power variability will be high, illustrated in Figure 2.1. The use of a variable speed PSH plant could then eliminate the need for multiple pump system by using one large instead, also preventing frequent starts/stop sequences when adjusting power output [5]. The implementation of variable speed PSH plants may prove a key technology for the further integration of non-dispatchable renewable energy sources into the power system, for example by preventing curtailment of wind power.

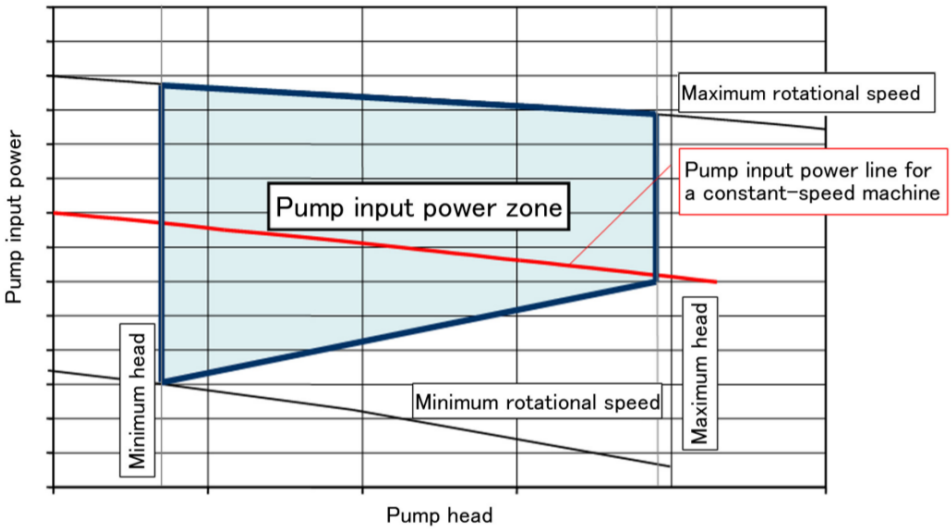

Figure 2.1: With variable speed technology, pumped-storage plants are able to adjust pumping power. Figure from: Mitsubishi Heavy Industries [1]

Furthermore, the market-oriented operation of power generation units also means that power output may be frequently adjusted and operation under partial loading in turbine mode is more common. Operating at partial loading will reduce the hydraulic efficiency of conventional fixed speed hydropower plants since turbines are designed for one optimum point at a specific head, discharge, unit size, and speed [8]. Also, pump-turbines are normally designed for optimal efficiency in pump-mode, further reducing the efficiency in turbine mode. By using variable speed motor-generators, the hydraulic efficiency at partial load can be improved with up to 10% by adjusting the speed according to the given head and discharge [7]. As many hydropower plants, including PSH plants, are in the hundreds of MW-scale, even small efficiency improvements will be an important contribution to the overall power system. As well as increasing efficiency, variable speed operation may

mitigate undesired hydraulic phenomena such as cavitation and vibration that occur under partial loading [9].

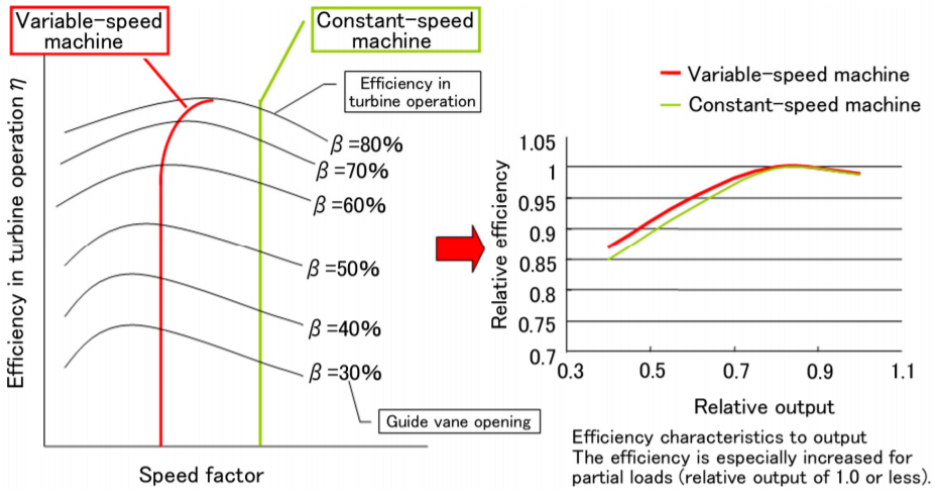

Figure 2.2: Variable speed operation allows higher operational efficiency than fixed-speed operation. Figure from: Mitsubishi Heavy Industries [1]

This thesis will investigate a pumped-storage hydropower system where variable speed operation is enabled by the use of a converter-fed synchronous machine (CFSM). By use of a full-sized frequency converter, the stator frequency is decoupled from the grid frequency such that the synchronous machine can be fed with variable voltage and frequency. Figure 2.3 presents an illustration of a CFSM configuration for a PSH plant where the stator terminals of the synchronous machine are connected to the grid through a back-to-back voltage source converter and an intermediate dc-link.

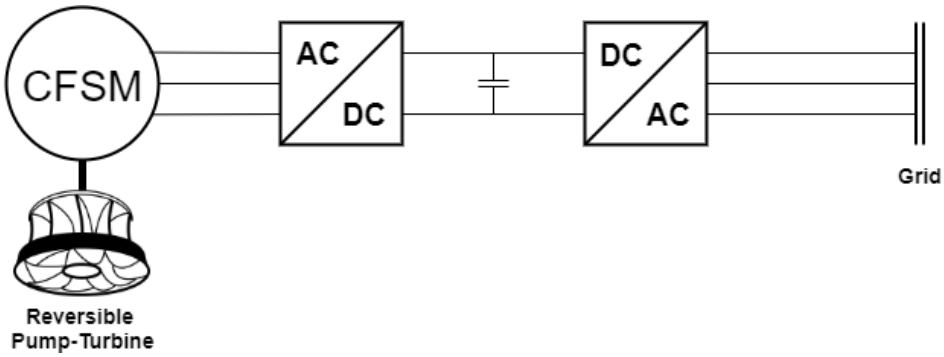

Figure 2.3: Illustration of a converter-fed synchronous machine configuration for variable speed hydropower.

Earlier implementations of variable speed hydropower plants have employed a technology called doubly-fed induction machine, where the rotor of an induction machine is fed by a frequency converter rated up to 30% of the machine rating. However, the developments in frequency converter technology have enabled full-sized frequency converters to be installed at up to 100 MW ratings. The advantages of the CFSM is superior performance in terms of speed variation, controllability and start-up procedure. Its drawback includes higher investment costs and increased power losses in the converter [5].

The use of frequency converters for variable speed operation provides the ability for high dynamic control of the power delivered to the grid, significantly faster than conventional plants where power output is controlled by the governor. In addition, by momentarily reducing the rotor speed, a large amount of active power can be injected to the grid from the kinetic energy of the rotor (*flywheel effect)*. The ability for instantaneous power injection is a useful contribution for improving power system stability. The adjustable speed range for hydropower applications is limited by the operational limits of the hydraulic system, starting from the lowest speed due to torque limitations and up to the runaway speed for the given guide vane opening, head and discharge. Practically, this enables a speed range of $\pm$ 30% of the rated speed [7]. In the Grimsel 2 PSH plant in Switzerland, one of the plants four turbine-pump units has been fitted with a full-sized frequency converter that enables a speed variation from 600 RPM to 765 RPM [10].

Chapter 3

System Modelling and Control

This chapter describes the modelling and control of the Converter-Fed Synchronous Machine (CFSM) system. An overview of the system can be seen in Figure 3.1, containing the essential components and parameters of the system. Matlab/Simulink 2019b [11] was used for the modelling and simulation of the CFSM system by using the Simscape Electrical block-library. The parameters of the system, its base values and implementation in Simulink can be found in Appendix B.1,B.2 and B.4 respectively.

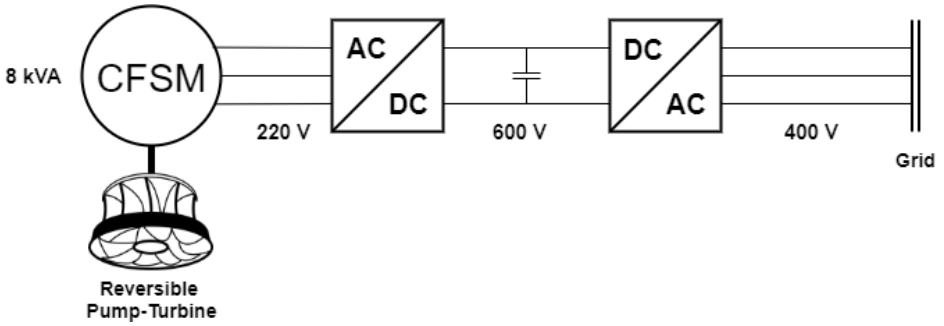

Figure 3.1: System overview of the variable speed hydropower plant.

3.1 Synchronous Machine

The synchronous machine model that is used is the *Synchronous Machine Salient Pole* modelled with standard pu values. The machine has a rating of 8 kVA with a terminal voltage of 220 V. The machine is based on a laboratory machine at NTNU and was thoroughly treated in a previous master thesis [2]. The machine is modelled with saturation, by implementing the saturation curve seen in Figure 8.1 of Appendix B.1.

3.2 Excitation System

The excitation system is modelled as a controllable voltage source controlled by the excitation system controller. The excitation system control strategy, which is presented later in Chapter 4, calculates a reference value of the field current and compares it to the actual field current of the machine. The error is sent through a PI-regulator and the output is finally fed to the controllable voltage source. The parameters of the excitation system can be found in Table 8.3 of Appendix B.1.

3.3 Hydraulic System

To represent both pump-mode and generator-mode, two different mechanical systems were created. A reversible Francis turbine in pump-mode can be modelled as a centrifugal pump [12], where the relation between power and speed is given as:

$$P_l = T_l \cdot \omega = k_t \cdot \omega^3 \tag{3.1}$$

The torque constant k_t is found by defining nominal power for nominal speed:

$$k_t = \frac{P_n}{\omega^3} = \frac{8000W}{(104.7rad/s)^3} = 6.97 \cdot 10^{-3}$$

To model a Francis turbine for power generation in studies involving large variations in power and frequency, Prabha Kundur's *Power Systems Stability and Control* [13] advice using a non-linear model of the hydraulic system. Therefore, a second-order hydraulic turbine and governor model was developed in Simulink. The model works based on a droop characteristic, determining the output power based on the deviation of the input frequency to a reference value. The parameters of the hydraulic turbine and governor model can be found in Table 8.4 of Appendix B.1. Due to the small size of the system, online sources were used to find parameter values of the turbine in generation-mode. The hydraulic system uses parameters from an 8 kW commercially available Francis turbine [14], while typical per-unit values for the governor were taken from *Power Systems Stability and Control* [13].

3.4 Converters and DC-link

The back-to-back converter consists of two voltage source converters (VSCs) connected through a dc-link. The sizing of parameters of the converters and dc-link was done by following the procedure found in [15], where a CFSM fed by a back-to-back VSC configuration was presented for use in wind power. The control setup of the converters were based on the classical torque control scheme found in literature [16]. The synchronous machine equations which was used for the converter control system can be found in Appendix A. The parameters of the converters and dc-link is found in Table 8.5 of Appendix B.1. Appendix B.3 lists the PI-regulator gains applied to the system controllers.

3.4.1 Control of Machine-Side Converter

The responsibility of the Machine-Side Converter (MSC) is to adjust the speed indirectly by controlling the electrical torque. This is done with two control loops, as seen in Figure 3.2: An outer control loop regulating the speed and an inner control loop regulating the currents. The output of the current control loop is a dq-voltage reference that is sent to the PWM which controls the converter switching.

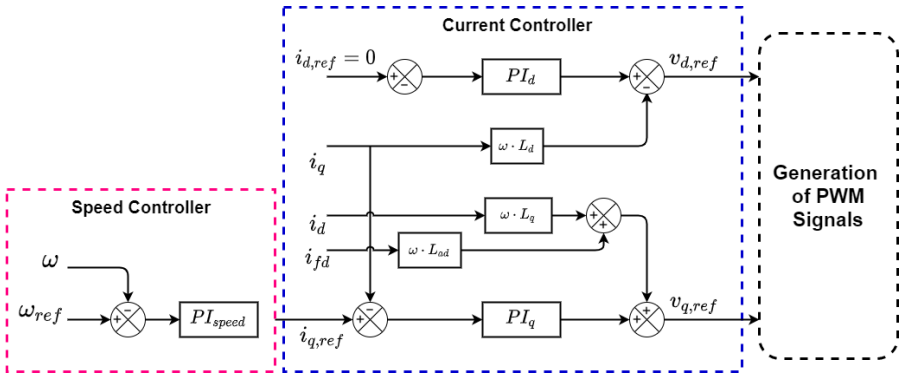

Figure 3.2: Machine-side controller loops.

The voltage equations for the synchronous machine (*Appendix A*) is the starting point for defining the inner current control loop of the machine-side converter:

$$\begin{bmatrix} v_d \\ v_q \end{bmatrix} = r_s \begin{bmatrix} i_d \\ i_q \end{bmatrix} + \frac{d}{dt}\begin{bmatrix} l_d \cdot i_d \\ l_q \cdot i_q \end{bmatrix} + l_{ad}\frac{d}{dt}\begin{bmatrix} i_{fd} \\ 0 \end{bmatrix} + \omega \begin{bmatrix} 0 & -l_q \\ l_d & 0 \end{bmatrix}\begin{bmatrix} i_d \\ i_q \end{bmatrix} + \omega \cdot i_{fd}\begin{bmatrix} 0 \\ 1 \end{bmatrix} \quad (3.2)$$

The voltage equations contain cross-coupling terms which must be eliminated for independent control of dq-axis variables. By using the decoupling terms defined in Equation 3.3-3.4, the current and dq-axis variables can be controlled independently. $\mathbf{PI_{d/q}}$ means PI-controller for d- and q-axis respectively.

$$v_{d,ref} = \mathbf{PI_d} \cdot (i_d^{ref} - i_d) - \omega \cdot l_q \cdot i_q \quad (3.3)$$

$$v_{q,ref} = \mathbf{PI_q} \cdot (i_q^{ref} - i_q) + \omega(l_d \cdot i_d + l_{ad} \cdot i_{fd}) \quad (3.4)$$

For the outer speed control loop, the starting point is the Swing Equation 8.19, giving the acceleration of the machine. By taking the load torque T_l as a disturbance, the machine's speed is controlled by regulating the electrical torque, T_e, defined in Equation 8.29. By assuming that the converter regulates the d-axis current to zero, the following expression for the electrical torque is obtained:

$$T_e = x_{ad} \cdot i_{fd} \cdot i_q \quad (3.5)$$

3.4.2 Control of the Grid-Side Converter

The Grid-Side Converter (GSC) controls the dc-link voltage and determines the flow of active and reactive power. The dc-link controller gives a reference value for the d-axis current such that the dc-link voltage is kept constant. Reactive power compensation is not implemented, such that the q-axis current reference is set to zero.

The grid-side equations of the system can be defined by the following equations [15]:

$$\begin{bmatrix} v_d \\ v_q \end{bmatrix} = r_{grid} \begin{bmatrix} i_d \\ i_q \end{bmatrix} + l_{grid} \frac{d}{dt} \begin{bmatrix} i_d \\ i_q \end{bmatrix} + \omega_g \cdot l_{grid} \begin{bmatrix} 0 & -1 \\ 1 & 0 \end{bmatrix} \begin{bmatrix} i_d \\ i_q \end{bmatrix} + \begin{bmatrix} v_d \\ v_q \end{bmatrix} \tag{3.6}$$

Where w_g is the electrical angular speed of the grid voltage, and r_{grid} and l_{grid} is the resistance and reactance of the transmission line and LCL-filter between the converter and the external grid.

Due to the cross-coupling terms $-w_g l_{grid} i_d$ and $w_g l_{grid} i_q$, the equations can be decoupled by the following equations:

$$v_{d,ref} = \mathbf{PI_d}(i_d^{ref} - i_d) + \omega_g \cdot l_{grid} \cdot i_q + v_d \tag{3.7}$$

$$v_{q,ref} = \mathbf{PI_q}(i_q^{ref} - i_q) + \omega_g \cdot l_{grid} \cdot i_d + v_d \tag{3.8}$$

Where $\mathbf{PI_{d/q}}$ again is the PI-controller for d- and q-axis current controllers.

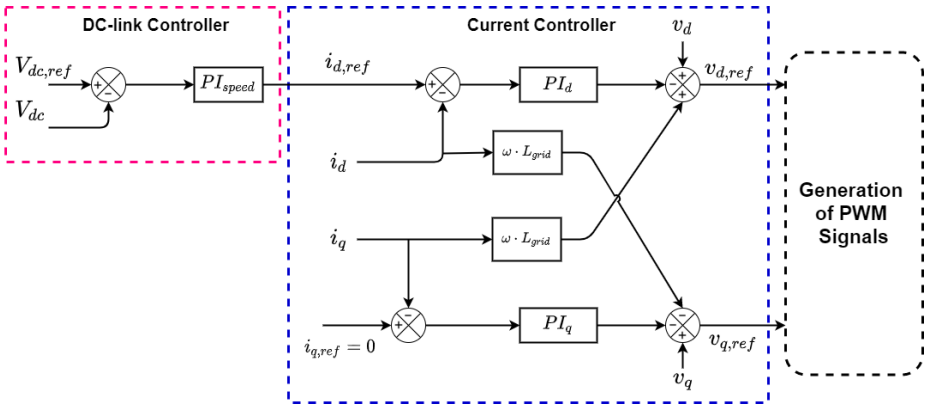

Figure 3.3: Grid-side controller loops.

The active and reactive power expressed in the dq-quantities of the grid are:

$$P_{ac} = v_d \cdot i_d + v_q \cdot i_q \tag{3.9}$$

$$Q_{ac} = -v_d \cdot i_q + v_d \cdot i_q \tag{3.10}$$

The dc-link voltage is controlled in the same way as the speed controller of the machine-side drive in Fig.3.2. The error between measured and reference dc-link voltage is sent through a PI-regulator to produce a reference value to the d-axis current. The d-axis voltage of the grid-side converter is aligned with the grid voltage by a PLL. The dc-link voltage is kept constant by regulating the flow of active power going in or out of the grid-side converter. Reactive power control is not implemented; Therefore the q-axis current reference is set to zero.

3.5 External Grid

The external grid is initially represented by an ideal voltage source in Chapter 4, but is later replaced by a synchronous machine in Chapter 5 when simulating frequency control of the pump load. The parameters of the synchronous machine used as a representation of the external grid in Chapter 5 can be found in Appendix D.4. Furthermore, an LCL-filter is placed between the grid-side converter and the external grid to reduce harmonics from the converter.

Complete Overview of System

The system described above is fully illustrated in Figure 3.4-3.5 for pump mode and generator mode respectively, with their controllers and variables.

Pump mode

In pump mode operation, the MSC regulates the speed of the machine and thus also the output power of the reversible pump-turbine. The GSC regulates the voltage of the dc-link by adjusting the flow of active power to and from the external grid and the CFSM. The excitation system will regulate the field current such that a 1.0 pu stator flux linkage is achieved, this strategy is explained in more detail in Chapter 4.

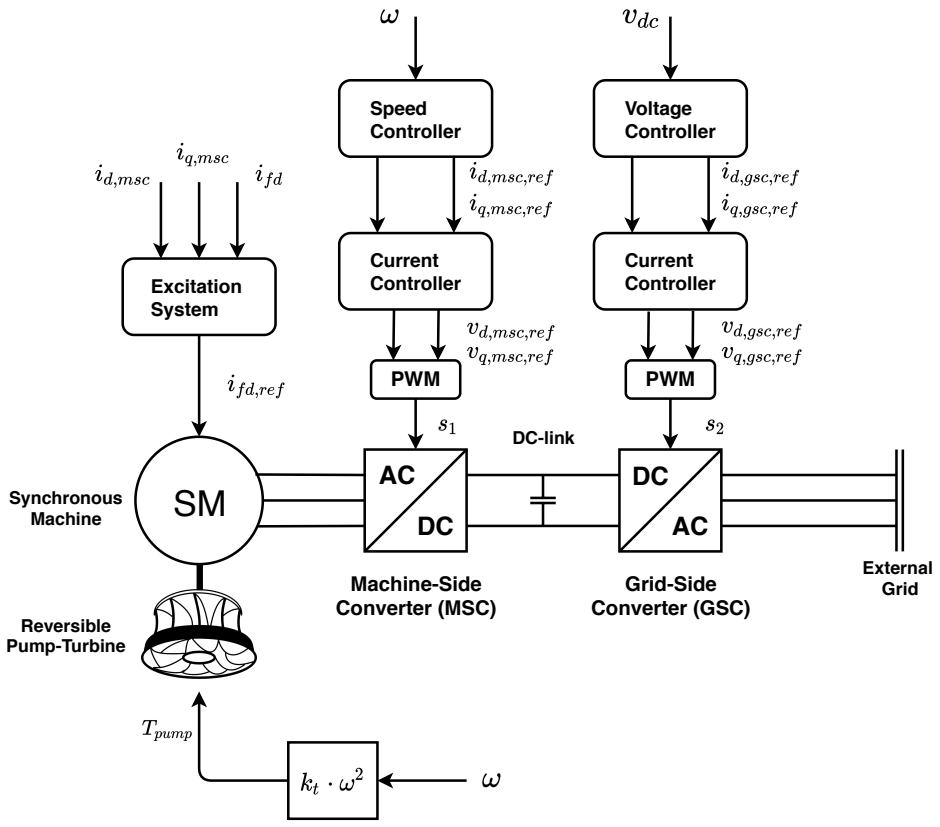

Figure 3.4: Overview of the variable speed hydropower CFSM in pump mode and its controllers.

Generator mode

In generator mode, the MSC and GSC have the same responsibilities as in pump mode, however, the power output of the turbine will depend on the regulation of the gate opening by the turbine governor, which determines the gate opening based on a frequency-droop characteristic. The Simulink implementation of the turbine and governor can be seen in Figure 8.5-8.6 of Appendix B.4.

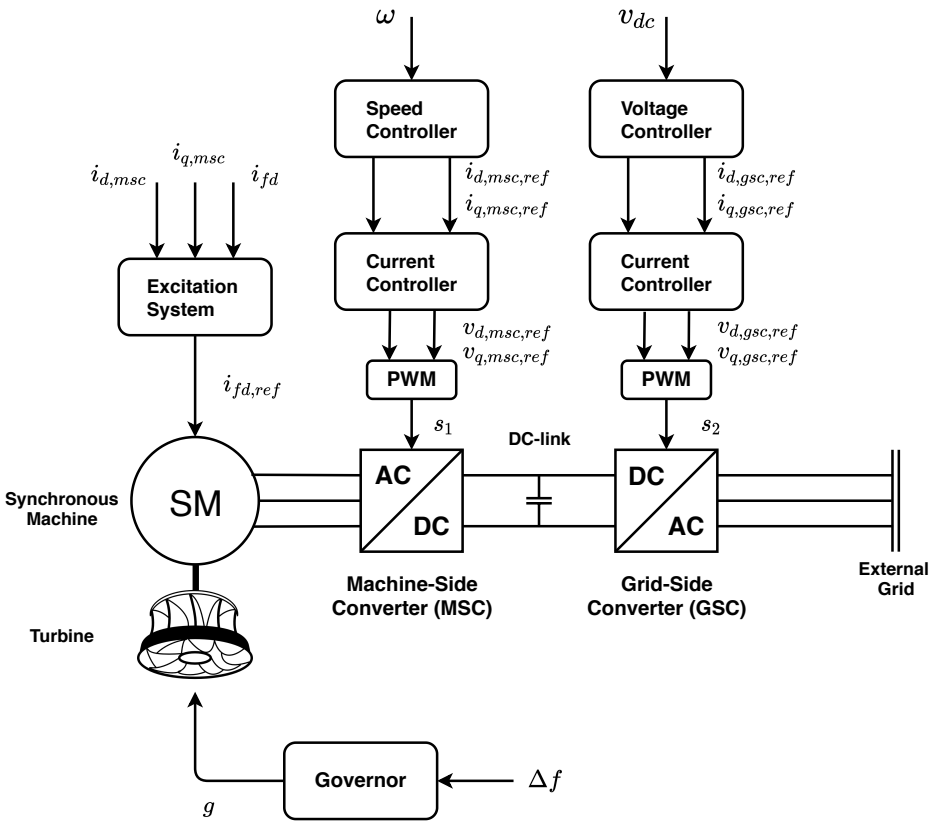

Figure 3.5: Overview of the variable speed hydropower CFSM in generator mode and its controllers.

Chapter 4

Excitation Control of the Synchronous Machine

This chapter will examine the control of the excitation system for the CFSM. Because separately excited CFSMs are fed with variable voltage and frequency from the converter, they possess one more degree of freedom compared to conventional hydropower plants. The decoupling of the stator and the external grid means that the excitation system of the CFSM can be used for another purpose than conventional AVR action. In Chapter 3, the electrical torque was defined by Equation 3.5 when the converter is regulating the d-axis current to zero. Equation 3.5 shows that the electrical torque is dependent on both the field current and the q-axis current, whose values are regulated by the excitation system and the machine-side converter respectively. In this chapter, the role of the excitation system will be analysed, with a focus on how the excitation system can be utilized to improve the operation of the CFSM.

4.1 Excitation System Control Strategy

Separately excited synchronous machine-drives are often controlled to operate with a unity power factor ($\cos\varphi = 1$), where the current and voltage waveforms are in phase [16]. A disadvantage of installing full-sized frequency converters in large hydropower plants is the associated converter losses. Some of the converter losses can be reduced by keeping the stator current low. If the stator current only contains a q-axis component, which it does with the machine-side control strategy presented in Chapter 3, the reduction in q-axis current needs to be compensated by increasing the field current to achieve the same electrical torque. However, a too high field current will saturate the machine which is also an undesirable way of operating the synchronous machine. To reduce the stator current as much as possible with the given converter control strategy, while at the same time prevent saturation of the machine, the excitation system will have the objective of regulating the stator flux linkage, Ψ_s, to 1.0 pu.

To accomplish this objective, the excitation system controller should seek to regulate the field current to a value that, given the d- and q-axis currents in the stator, produces the desired stator flux linkage of 1.0 pu.

The calculation of the field current reference is based on the relation described in Equation 4.1:

$$\Psi_s = \sqrt{\psi_d^2 + \psi_q^2} \tag{4.1}$$

The dq-axis flux linkages, in per-unit, can be expressed further as:

$$\psi_d = x_{ad} i_{fd} + x_d i_d = x_{ad} i_{fd} + (x_{ad} + x_l) i_d \tag{4.2}$$

$$\psi_q = x_q i_q = (x_{aq} + x_l) i_q \tag{4.3}$$

In salient pole synchronous machines, it is often assumed that q-axis mutual inductance does not saturate, mainly because the q-axis flux is usually quite small in comparison to the d-axis flux [13]. Therefore, x_{aq} is assumed to be constant, independent of the magnetization of the machine such that x_q can be used as a constant parameter in the next equations.

By inserting Equation 4.2 and 4.3 into Equation 4.1:

$$\Psi_s = \sqrt{(x_{ad} i_{fd} + (x_{ad} + x_l) i_d)^2 + (x_q i_q)^2} \tag{4.4}$$

By solving for the field current, the following equation is obtained:

$$i_{fd} = \frac{1}{x_{ad}} \sqrt{\Psi_s - (x_q i_q)^2} - \frac{x_{ad} + x_l}{x_{ad}} i_d \tag{4.5}$$

By regulating the field current according to Equation 4.5, the stator flux linkage can be kept at 1.0 pu. The different variables comprising Equation 4.5 are: two, assumed to be, constant variables x_q and x_l, the dq-axis currents regulated by the machine-side converter, the stator flux linkage reference which is set to 1.0 pu and finally the d-axis mutual inductance that is dependent on the saturation of the machine. In the next section, the effect of saturation on the d-axis mutual inductance will be analysed.

4.2 Effects of Saturation

Saturation is often neglected in system studies [17], but its effect will in indeed change the values of mutual inductances of the machine. The consequence of using the unsaturated value will be that an erroneous field current reference is calculated, leading to a non-unity power factor. A more accurate calculation of the field current reference would be achieved if measurements of the mutual fluxes or inductances were available. Equation 4.1-4.5 are defined by reactances; However, the system model Simulink uses d-axis mutual inductance l_{ad} instead. As per-unit values are used, these two parameters take on the same values.

In the Simulink model, a challenge is that even though saturation is taken into account in the synchronous machine model, the mutual fluxes are not available as measurements in Simscape Electrical's synchronous machine model. Simscape Electrical [18] was used in the complete variable speed PSH plant presented in Chapter 3, because of the easier implementation of the mechanical part of the variable speed PSH plant. However in another Simulink library, the Specialized Power System toolbox, the synchronous machine model will provide the mutual inductances as measurements [19]. Therefore, it was assumed that since the synchronous machine model found in Simscape Electrical and Specialized Power System uses the same sixth-order state-space representation, the behaviour of the mutual inductance under saturation in Simscape Electrical would be similar to what is observed in Specialized Power Systems.

To examine the accuracy of field current reference calculation when assuming unsaturated parameters, the following test case was analysed: The 8 kVA synchronous machine presented in Chapter 3 swinging against an ideal three-phase voltage source. The Simulink model can be found in Appendix C. The objectives of this analysis were to:

(A) Investigate the effect of saturation on the d-axis mutual inductance, l_{ad}, of the synchronous machine when varying the available input variables to the machine.

(B) Examine the accuracy of assuming constant mutual inductance when estimating the stator flux.

(C) If possible, improve the stator flux estimation by taking into account the effects of saturation.

Part A: Effect of saturation on mutual inductances

The synchronous machine model was implemented with the saturation curve seen in Figure 8.1 of Appendix B.1. The effect of changing the two input variables to the machine model was examined: the power and the field voltage. The first test considered the following input to the machine model: 0.6 pu input mechanical power and a field voltage that was stepped from 0.8 pu to 1.5 pu. From Figure 4.1 it can be seen that the d-axis mutual inductance will decrease for a step in the field voltage. Before the step in field voltage is applied, the d-axis mutual inductance takes on the unsaturated value at 0.58 pu. However, after increasing the field voltage, the d-axis mutual inductance will decrease to 0.532 pu.

The second test considered the following input to the machine model: 1.0 pu field voltage while the generated power was stepped up from 0.4 pu to 1.0 pu. Figure 4.2 shows how the d-axis mutual inductance will increase towards its unsaturated value as the power is increased. However, the change in the d-axis mutual inductance parameter is rather small for this step relative to the step in field voltage earlier. The observed oscillations are a consequence of the oscillating d-axis current after the load step.

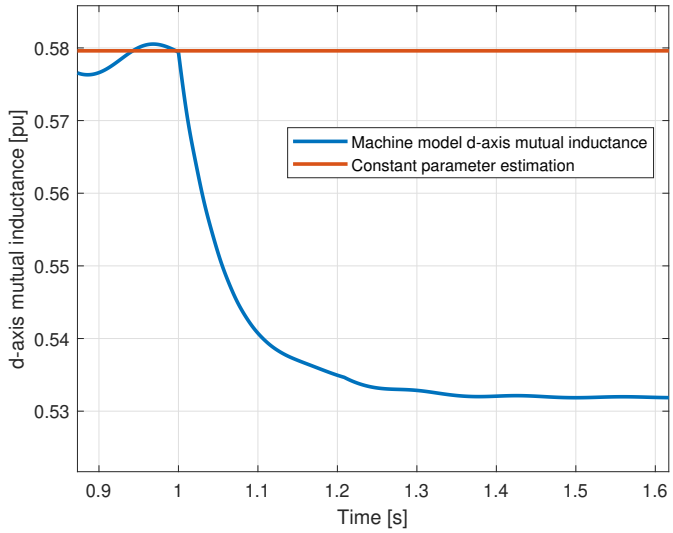

Figure 4.1: d-axis mutual inductance for step in field voltage from 0.8 to 1.5 pu. The machine is operating at nominal speed and an output power of 0.6 pu.

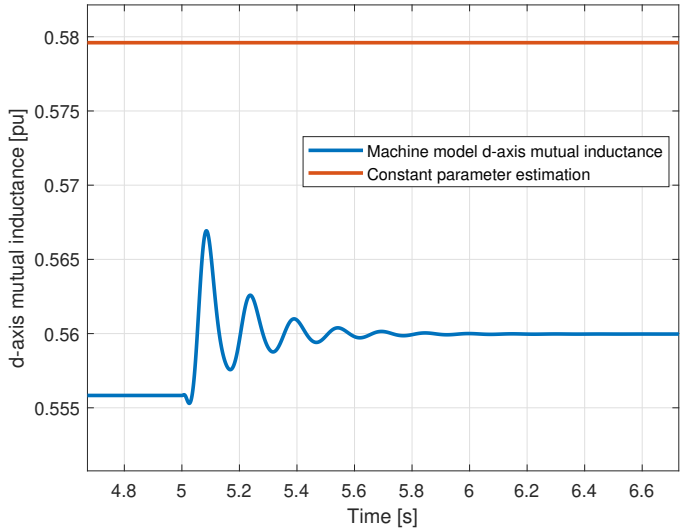

Figure 4.2: d-axis mutual inductance for step in power from 0.4 to 1.0 pu. The machine is operating at nominal speed and an input field voltage of 1.0 pu.

The results confirm that the d-axis mutual inductance varies according to the magnetization of the machine, again dependent on the field and d-axis current. Pyrhönen et. al [20] analysed saturation from the excitation system point of view and stated that the saturated mutual inductances must be modelled as functions of the currents on both magnetic axes. As mentioned previously, only the saturation of the d-axis mutual inductance will be modelled, as Simulink itself assumes the q-axis mutual inductance to be a constant parameter. This is an additional assumption often made, simply because q-axis flux is usually rather small when compared to the d-axis flux due to the effect of the field winding [17].

Part B: Accuracy of constant parameter assumption

Part A of this analysis indicated that the saturation of the machine may affect the value of the d-axis mutual inductance of the machine model significantly, thus the calculation of the field current reference will not be accurate for operation of the machine in saturation. Using unsaturated values will overestimate the stator flux linkage, as shown in Figure 4.3-4.4, where the estimated stator flux is plotted against the stator flux linkage from the machine model. Applying a step in the field voltage will sharply reduce the accuracy of the estimation, from approximately zero to 7.4 % error. On the other hand, applying the power step in Figure 4.6 is seen to affect the accuracy of the estimation to a lesser degree, where a decrease in error from 3.4 % to 2.65 % is observed.

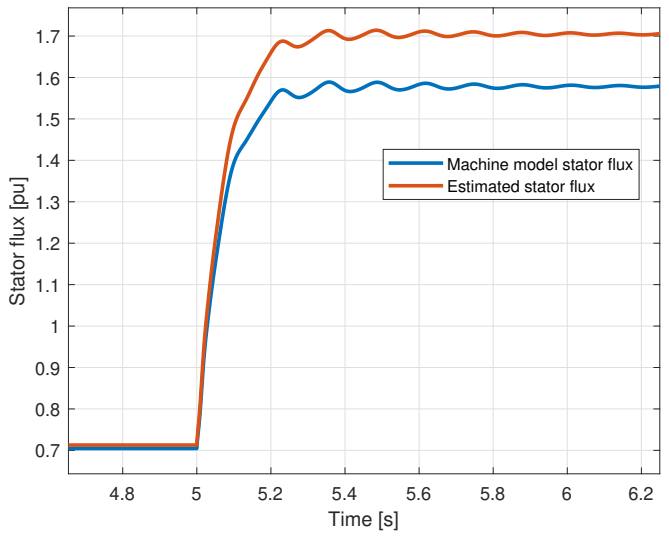

Figure 4.3: Accuracy of the stator flux linkage estimation for step in the field voltage from 0.8 to 1.5 pu. The machine is operating at nominal speed and an output power of 0.6 pu.

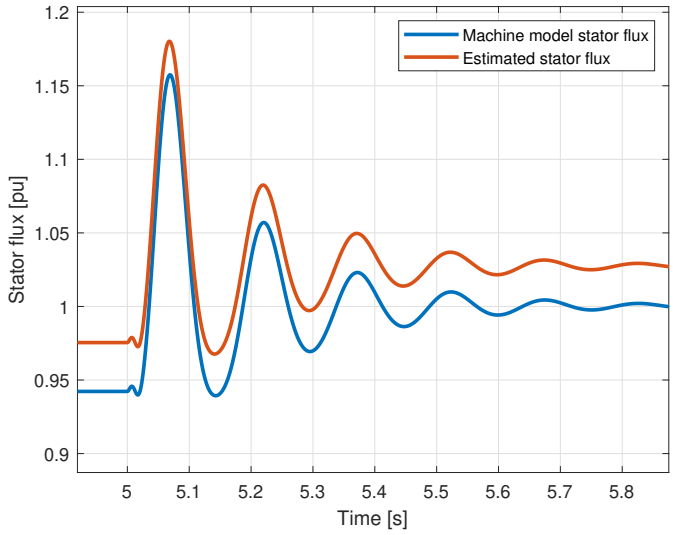

Figure 4.4: Accuracy of the stator flux linkage estimation for step in input power from 0.4 to 1.0 pu. The machine is operating at nominal speed and an input field voltage of 1.0 pu.

Part C: Taking saturation into account

The two tests indicated that l_{ad} depends on both field voltage and input power, which are the two input variables to the machine model. A step in power will affect the d-axis current, while a step in field voltage will affect both field current and d-axis current. Literature sources on modelling of saturation effects on synchronous machine drives suggests defining a magnetization current $i_m = i_{fd} + i_d$ [20]. For varying operating conditions, this value is logged together with the d-axis mutual inductance, such that l_{ad} is expressed as a function of i_m. Data-points of l_{ad} for varying field voltage and input power was obtained through simulations, and later used in the Curve Fitting Toolbox [21] in Matlab to approximate a linear function for l_{ad} (*Appendix C Figure 8.16*). The obtained function is defined by Equation 4.6 below:

$$l_{ad}(i_m) = 0.6 - 0.011 \cdot i_m \tag{4.6}$$

In Simulink, a saturation block is added to the implementation to prevent the approximated inductance to exceed the unsaturated value. A too low value of the inductance, for high i_m, is limited by the ceiling voltage of the excitation system's PI-regulator and the drive's control system. To verify the accuracy of the d-axis mutual inductance estimation, the following two tests were performed: constant power - step in field voltage and constant field voltage - step in power. The results can be seen in Figure 4.5-4.6. When stepping the field voltage to 1.5 pu, the difference between the machine model stator flux linkage and the constant parameter assumption will increase. On the other hand, the parameter estimation based on Equation 4.6 will predict the d-axis mutual inductance with reasonable

accuracy both before and after the load step. It is observed that for $\Psi_s < 1.0$ pu, the constant parameter assumption will underestimate the stator flux linkage, while it will overestimate it for $\Psi_s > 1.0$ pu. The step in output power, which indirectly changes the dq-axis currents, does not change the accuracy of the estimation techniques noteworthy. For a converter-fed synchronous machine with classical torque control, the d-axis current will anyway be regulated to zero by the current controller.

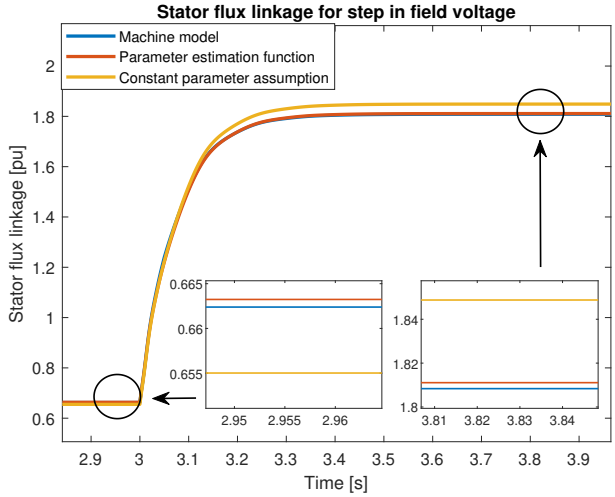

Figure 4.5: Comparison of improved and initial stator flux estimation for a constant power of 0.8 pu and a step in field voltage from 0.8 pu to 1.5 pu. Mechanical speed is held constant at 1.0 pu.

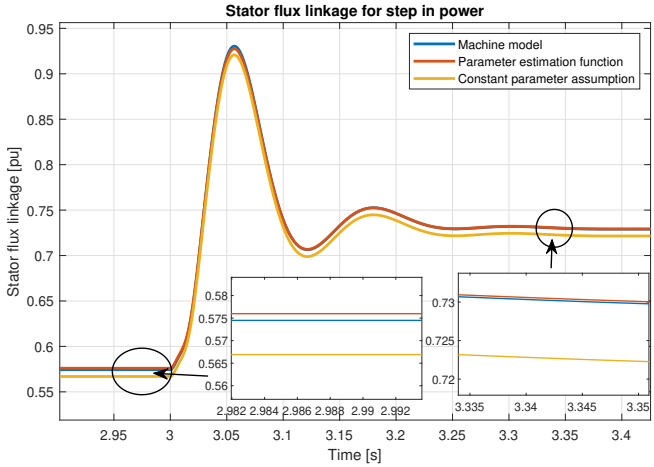

Figure 4.6: Comparison of improved and initial stator flux estimation for a constant field voltage of 0.8 pu and a step in power from 0.4 pu to 1.0 pu. Mechanical speed is held constant at 1.0 pu.

4.3 Implementation of $\Psi_s = 1$ Control Strategy

The block diagram of the proposed excitation system controller can be seen in Figure 4.7. Before this step, l_{ad} is calculated from Equation 4.6 based on the measured $i_m = i_{fd} + i_d$. The dq-axis and field -current measurements are filtered with a low pass filter with a time constant of 0.2 ms. The approximated value of the saturated l_{ad} is used in the calculation of the field current reference by Equation 4.5, which calculates the field current that will ensure $\Psi_s = 1$ pu. The field current reference value is compared to a measurement of the field current from the machine. The error is sent to a PI-regulator, providing a reference to a controllable voltage source. The complete implementation of this controller in Simulink can be seen in Figure 8.17-8.20 of Appendix C.

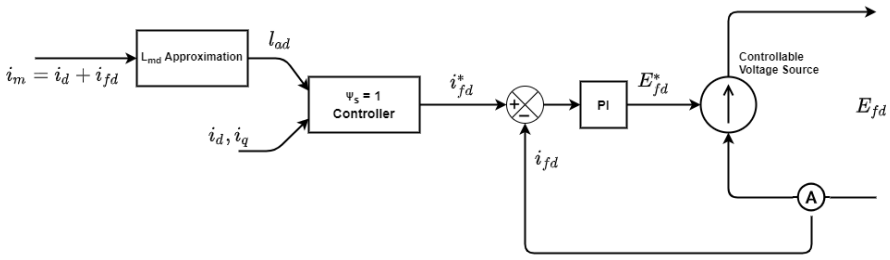

Figure 4.7: Block diagram of the excitation system control strategy.

4.4 Analysis of $\Psi_s = 1$ Strategy

The desired outcome of the $\Psi_s = 1$ pu strategy is to achieve maximum torque per ampere, i.e. to reduce the current losses in stator and converter, as well as ensuring optimal use of the CFSM. The control method implemented in the previous section will now be compared to controlling the field current to its rated value, along with simulations with 1.5 and 2.0 pu field current. The CFSM system described in Section 3 was used for comparing the control strategies. The test case concerns a synchronous machine operated in pump mode, which ramps its pump load from 0.5 to 1.0 pu. This is done by changing the speed reference of the MSC controller from 0.78 to 1.0 pu. To produce better and more visible plots, a low pass filter of 2 ms was used on all the measured quantities to remove noise. The results from this test case can be found in Chapter 6.1. The base field current is defined in the Simulink model as $i_{fd,base} = i^*_{fd} \cdot x_{ad,unsat}$, where i^*_{fd} is the field current that gives 1.0 pu voltage at no-load. Therefore, Equation 3.5 from Chapter 3 needs to be modified when calculating the torque for this analysis:

$$T_e = x_{ad,sat} \cdot i_{fd,0} \cdot i_q = x_{ad,sat} \cdot \frac{i_{fd}}{x_{ad,unsat}} \cdot i_q = \frac{x_{ad,sat}}{x_{ad,unsat}} \cdot i_{fd} \cdot i_q \tag{4.7}$$

Chapter 5

Control Strategies for Variable Speed Hydropower

PSH plants may prove to be an important enabler of renewable energy sources, being able to store energy and support the grid with auxiliary services. With variable speed technology, the PSH plants can operate with power control in pumping mode, a function which conventional, direct grid-connected plants are unable to perform. In addition, fast power injections can be provided by reducing the rotor speed or the dc-link voltage. This chapter will examine the auxiliary services that can be provided by the PSH plant presented in Chapter 3.

In the next sections, the following aspects of a variable speed PSH plant will be investigated:

Scenario A: Power control in pump mode.

Scenario B: Frequency control of pump load.

Scenario C: Synthetic inertia control.

5.1 Scenario A: Power Control in Pump Mode

Scenario A will examine the role of PSH as a variable load to be used in a power system influenced by intermittent energy sources such as wind power, illustrated in Figure 5.1. PSH plants in combination with wind power is becoming an attractive solution because surplus energy can be stored and dispatched in times of low wind power generation [22][23]. In addition, it will be beneficial for the grid to observe a constant power from the wind power source, without fluctuations in power [24].

The power fluctuations from the wind power source can be compensated by setting the PSH plant to adjust its pumping power according to the difference between forecasted and actual wind power:

$$P_{pump} = P_{base} + P_{wind} - P_{forecast} = P_{base} + \Delta P_{wind} \tag{5.1}$$

The PSH plant will under forecasted wind conditions pump with a constant base-load, P_{pump}. However, if the available wind power increases, the PSH plant will change its pumping power to accommodate for the amount available of power in the grid. In the simulation model presented in Chapter 3, the reversible pump-turbine is modelled as a centrifugal pump where the power output is dependent on the machine speed:

$$P_{pump} = K_t \cdot \omega^3 \tag{5.2}$$

This means that the regulation of pumping power will be done by regulating the speed reference to the control system of the MSC. The speed reference is calculated by Equation 5.3:

$$\omega_{ref} = \sqrt[3]{P_{base,pu} + \Delta P_{wind,pu}} \tag{5.3}$$

This must abide the operational limits of the PSH plant. A relevant example is the Grimsel 2 variable speed PSH plant in Switzerland, where the plant is able to regulate pumping power within the speed interval of 600-765 RPM [10]. Assuming a centrifugal pump model, such as the one used in this thesis, this corresponds to approximately a 0.8-1.0 pu speed regulation or a 0.5-1.0 pu regulation in power, assuming that 765 RPM is the nominal speed. Operation points outside these limits will produce undesired hydraulic phenomena such as pressure and torque pulsations [9].

The system described in Chapter 3 is used to represent the PSH plant, while the variable power output from the wind source can be seen in Figure 5.2. The nominal power of the wind power source is 20 kW or 2.5 per unit of the base machine power. A delay of 1 second in-between each new update of the power set-point is used. The wind power output that can be seen in Figure 5.2 is given a new value every 0.1 seconds which is taken as ”in real time” for this scenario. For every 0.1 seconds, the wind power output is allowed to deviate from its previous value with up to 300 W or 1.5 % of the nominal wind power output of 20 kW.

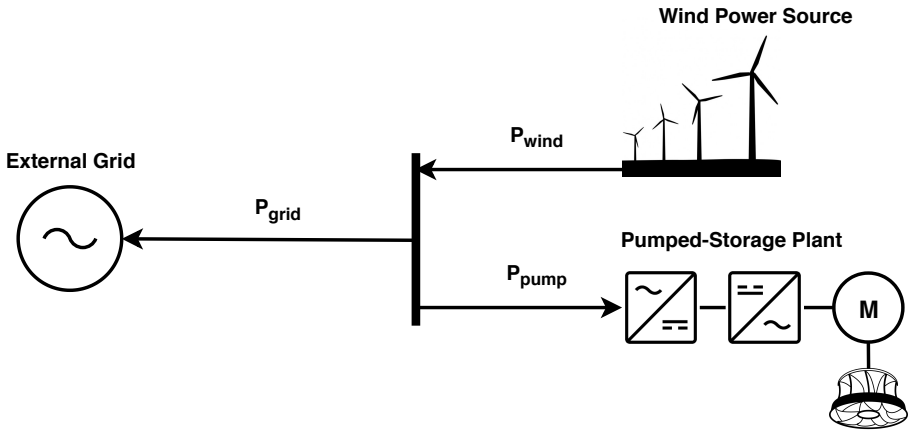

Figure 5.1: Illustration of the system in Scenario A.

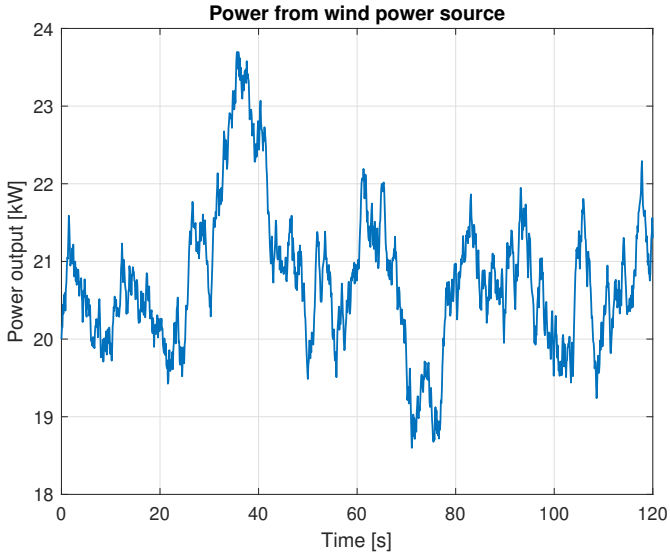

Figure 5.2: The assumed power output measured from the wind power source in Scenario A.

5.2 Scenario B: Frequency Control of Pump Load

The PSH plant can be controlled to take part in the frequency regulation of the power system by implementing a frequency droop characteristic on the pump load. By using the PSH plant as a frequency-controlled load, the power system's frequency response to disturbances can be improved [24]. In power systems with a large share of coal-fired or nuclear power plants, such as the Japanese, variable speed PSH plant have successfully been used to take part in load balancing and frequency regulation [25]. Frequency droop control may also be of use for weak or isolated grids, especially with low loads and variable generation [26].

Scenario B will examine the use of the PSH plant as a frequency controlled load, in a grid maintained by a 80 kVA synchronous machine with steam turbine as its prime mover. An AVR connected to the 80 kVA machine, which regulates the voltage to 400 V. The external loads consists of a 40 kW base load and a variable load varying as seen in Appendix D.3. Figure 5.3 illustrates the setup of the simulation model.

To implement a frequency control scheme of the plant's pumping power, the power set-point reference is calculated in Equation 5.4 by comparing the measured grid frequency with the nominal frequency. The relation between grid frequency and power set-point of the pump load is illustrated in the droop-characteristic found in Appendix D.1.

$$P_{pump,ref} = P_{base} - K_d(f_n - f_{grid}) \tag{5.4}$$

The speed reference to the outer speed control loop of the MSC is calculated by Equation 5.3. The complete Simulink implementation can be found in Appendix D.2. The frequency-controlled pump load is compared against a base case, where the PSH plant is operated as a constant load set to 0.75 pu of the PSH rated power.

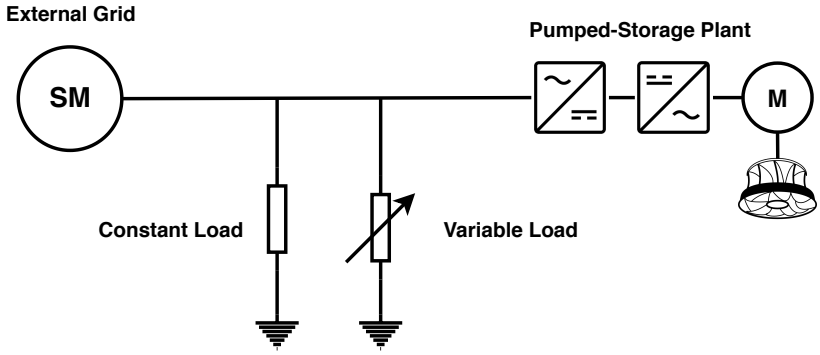

Figure 5.3: Illustration of the system in Scenario A.

5.3 Scenario C: Synthetic Inertia

Minor disturbances in the power system are normally dampened by large synchronous machines with substantial rotational inertia that limits the rate of change of the grid frequency. A consequence of the implementation of variable speed hydropower by CFSMs is that the total inertia of the power system is reduced. This inertia can be emulated by the plant control scheme, in what is often termed synthetic or virtual inertia.

Energy stored in the rotor

For instantaneous power injection, the kinetic energy stored in the rotor can be utilized, seen by Equation 5.5-5.6. By reducing the rotor speed during transients, power can quickly be injected to the grid. For sharper de-acceleration (*low dt*), the initial power spike is higher, but last shorter than for slower de-acceleration ramps. This is shown in Figure 5.4, where the speed is reduced from 1.0 pu to 0.7 pu.

$$E_{rotor} = \frac{1}{2} \cdot J \cdot \omega^2 \tag{5.5}$$

$$P_{rotor}dt = E_{rotor,1} - E_{rotor,2} = \frac{1}{2} \cdot J \cdot (\omega_1^2 - \omega_2^2) \tag{5.6}$$

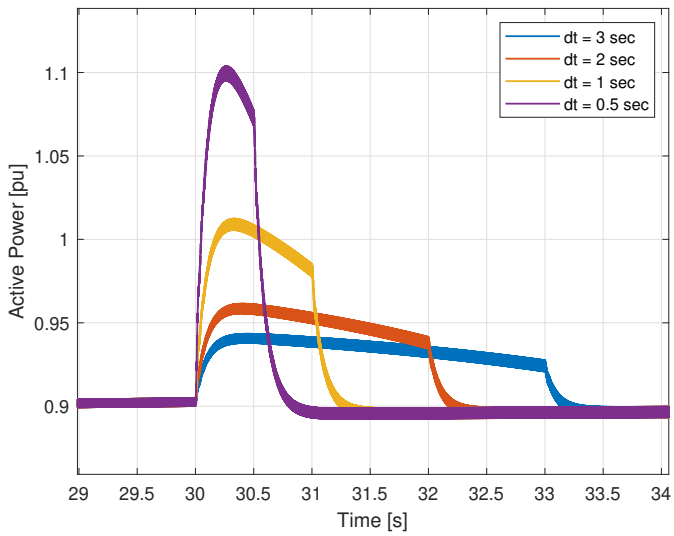

Figure 5.4: Power output from grid-side converter showing instantaneous power injection from rotational energy for different de-acceleration ramps, dt, when the speed is reduced from 1.0 pu to 0.7 pu. The inertia time constant of the machine is 0.205 s.

The instantaneous power injection from the rotor can be seen as a one-time use, temporary measure to reduce the initial frequency drop during contingencies. In the same way, during load rejection (*loss of load*), the speed can be increased to quickly absorb power from the grid. Practically, the speed range should carefully be constrained to $\pm 25\%$ of the optimum speed for the current operating point to avoid pressure pulsations and random flow phenomena [7]. The utilization of the rotational energy can be a way of compensating for the slower dynamics of the hydraulic turbine and governor which will need more time to ramp up or down its power output.

From a control perspective, the power injection from the rotor can be controlled by modifying the q-axis current reference or the speed reference. From a previous master's thesis it was discovered that influencing the speed reference gives a lengthier power boost than influencing the q-axis current reference [2]. Therefore, it is desired to influence the speed reference to achieve a lengthier power response, such that less governor action and ramping of turbine power is required. For larger frequency drops, requiring fast power injection and additional ramping of power, the instantaneous power injection could also be able to cover some of the power generation deficit while the hydraulic system is increasing its power output.

The power injection can be controlled such that it acts on changes in the grid frequency by using a derivative controller. However, this will cause power fluctuations as the derivative of the frequency will change as the initial drop in frequency is stopped and brought back to nominal frequency. Therefore, it is desirable to reduce the rate of which the speed is brought back to its former operating speed until the nominal frequency is restored. This challenge can be solved by adding a droop term to the controller. The implementation of the controller can be seen in Figure 5.5.

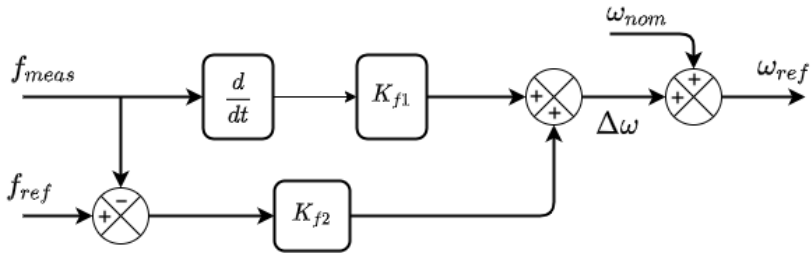

Figure 5.5: Rotor inertia controller.

The test case for the rotor inertia controller is a PSH plant connected to an external grid as seen in Figure 5.3 from Scenario B. The base load of the system is 40 kW and at t = 20 seconds an 8 kW load is connected. The pumped storage plant is operated at rated power. The rotor-inertia controller is compared against a PSH plant without a rotor inertia controller. The parameters of inertia controller is $K_{f1} = 0.05$ and $K_{f2} = -0.5$. Further thoughts on the creation and tuning of this controller is presented in Appendix E.

Energy stored in the dc-link

Another component of the CFSM system that contains quickly dispatchable energy is the dc-link capacitor, given by Equation 5.7-5.8. Synthetic inertia from the dc-link capacitor has been proposed as a solution to emulate inertia in PV systems [27].

$$E_{dc} = \frac{1}{2} \cdot C_{dc} \cdot V_{dc}^2 \tag{5.7}$$

$$P_{dc}dt = E_{dc,1} - E_{dc,2} = \frac{C_{dc}}{2} \cdot (V_{dc,1}^2 - V_{dc,2}^2) \tag{5.8}$$

The amount of energy provided by the dc-link will be limited by the minimum allowable dc-link voltage. Based on [15], the dc-link voltage should at minimum be:

$$v_{dc} = x\frac{2}{\sqrt{3}} \cdot V_{line,rms} \tag{5.9}$$

Where x is the over-voltage factor, set to 1.1 for low voltage systems [15]. Using the grid-side 400 V as line voltage, this gives a lower limit of approximately 500 V of the dc-link. When the nominal dc-link voltage is 600 V, the instantaneous power injections seen in Figure 5.6 can be obtained for a range of dt's. The rated stored energy in the dc-link is 1180 J. With a minimum dc-link voltage of 500 V, the allowable amount of energy that can be released is 363 J.

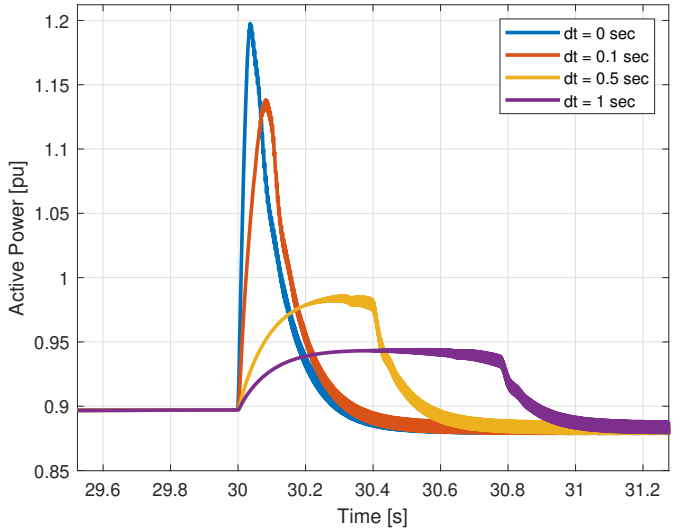

Figure 5.6: Power output from grid-side converter showing instantaneous power injection from dc-link capacitor different de-acceleration ramps, dt. Machine speed in this illustration is set to 1.0 pu.

The fast dispatchable energy from the capacitor will be controlled by an inertia controller based on a frequency droop. The controller will only act for a frequency deviation above

or under 0.1 Hz which is done by applying a dead zone to the controller. From the tuning of the capacitor inertia controller in Appendix F, it was found that for droop constants from $K_d = -200\frac{V}{Hz}$ and higher, the contribution to the frequency response will reach a limit where it cannot contribute more. Therefore, the lowest value, $K_d = -200\frac{V}{Hz}$, is used. The test case presented and discussed in Section 6.4 and 7.2 is the same as the one described for the rotor inertia controller.

Chapter 6

Results

6.1 Excitation System Control Strategy

Table 6.1: Measured d-axis mutual inductance from the test case of Sec. 4.4.

Control strategy	d-axis mutual inductance
$i_{fd} = 1.0$ pu	0.5670 pu
$i_{fd} = 1.5$ pu	0.5605 pu
$i_{fd} = 2.0$ pu	0.5540 pu
$\Psi_s = 1.0$ pu	0.5570 pu
	(0.5575 pu after load step)
$l_{ad,unsat}$	0.5796 pu

The q-axis current before and after the load step was measured for each control strategy, and can be found in Table 6.2 below. The d-axis current where for all cases properly regulated to zero, with only minor fluctuations above/below its zero-reference. After the load step is applied, the q-axis current will change due to receiving a new current reference by the speed control loop in Figure 3.2. For all control strategies, the q-axis current is instantly changed to 1.0 pu, which is the upper limit of the dq-axis current reference in the current controller. In steady-state, after the speed set point is reached, the q-axis current will settle at a new, higher value.

Based on Table 6.2, the torque per ampere (TPA) for each control strategy was calculated at full load:

$$TPA = \frac{|T_{e,fl}|}{|i_s|} = \frac{|T_{e,fl}|}{|i_{q,fl}|} = \frac{1.0pu}{|i_{q,fl}|}$$

Control strategy	i_q [pu]	TPA
$i_{fd} = 1.0$ pu	$0.509 \rightarrow 0.848$	1.179
$i_{fd} = 1.5$ pu	$0.408 \rightarrow 0.671$	1.490
$i_{fd} = 2.0$ pu	$0.346 \rightarrow 0.565$	1.770
$\Psi_s = 1.0$ pu	$0.374 \rightarrow 0.621$	1.610

Table 6.2: Torque-per-Ampere ratio and q-axis current as load is stepped from 0.5 pu to 1.0 pu.

Figure 6.1-6.2 presents the differences in q-axis current and stator flux linkage respectively. In Figure 6.3, the speed during the load step of the different control strategies can be seen. Finally, Figure 6.4 shows the field current as a function of time for the $\Psi_s = 1.0$ pu strategy.

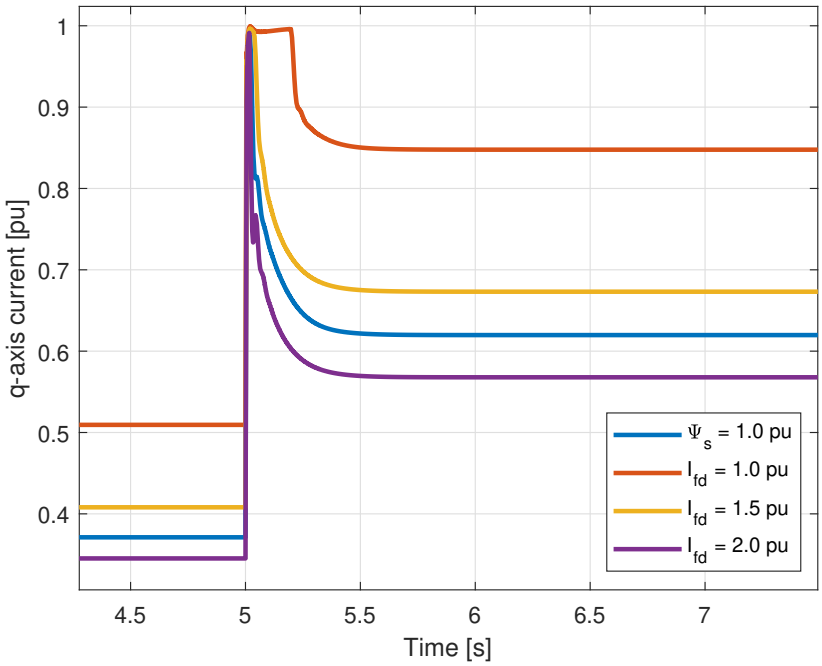

Figure 6.1: The q-axis currents for a load step from 0.5 pu to 1.0 pu (speed reference change from 0.78 pu to 1.0 pu).

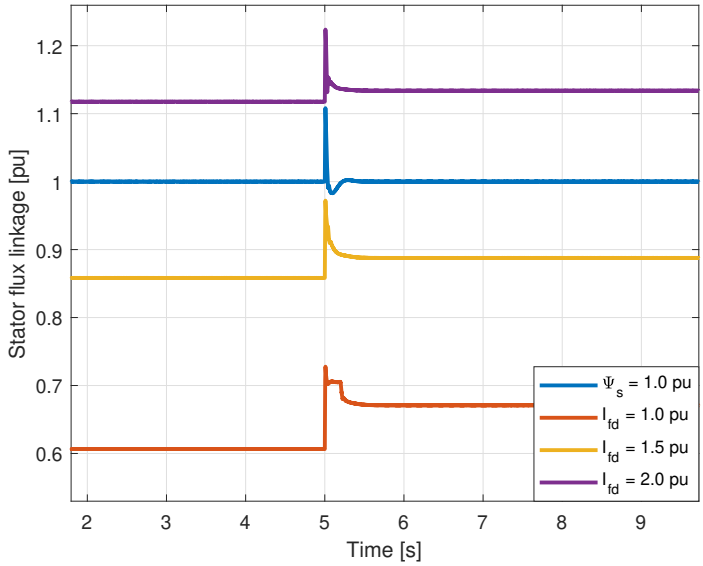

Figure 6.2: The stator flux linkages for a load step from 0.5 pu to 1.0 pu (speed reference change from 0.78 pu to 1.0 pu).

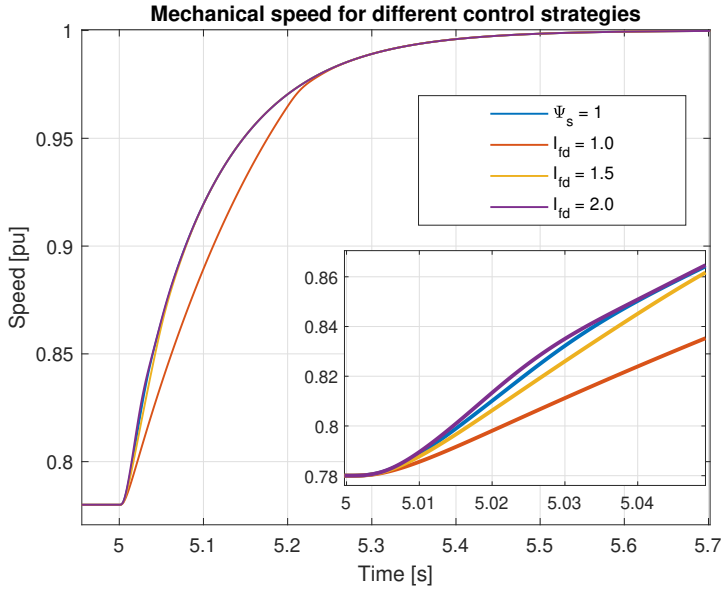

Figure 6.3: Transition time from 0.78 pu to 1.0 pu speed of the machine. This equals an increase from 0.5 pu to 1.0 pu in pumping power.

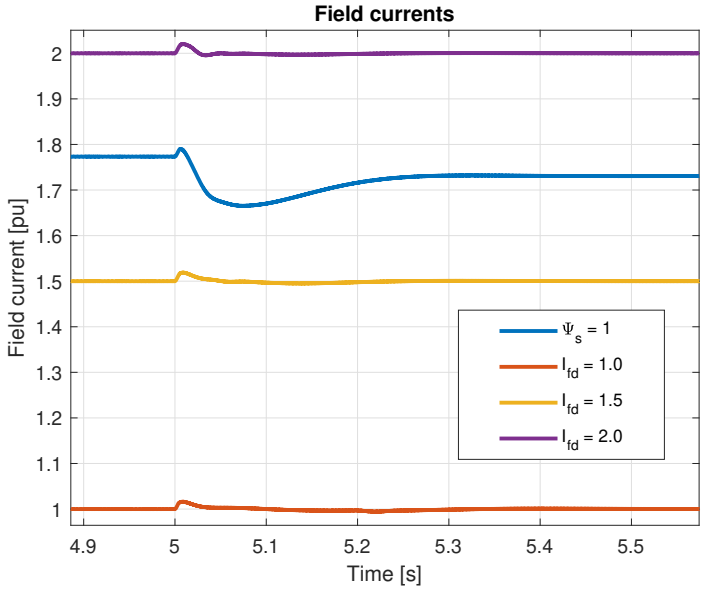

Figure 6.4: The field currents of the different control strategies as a function of time, given a load step from 0.5 pu to 1.0 pu (speed reference change from 0.78 pu to 1.0 pu).

6.2 Scenario A: Power Control in Pump Mode

The wind power source is normalised in per-unit quantities with the machine base power such that 20 kW nominal wind power equals 2.5 pu in machine base power.

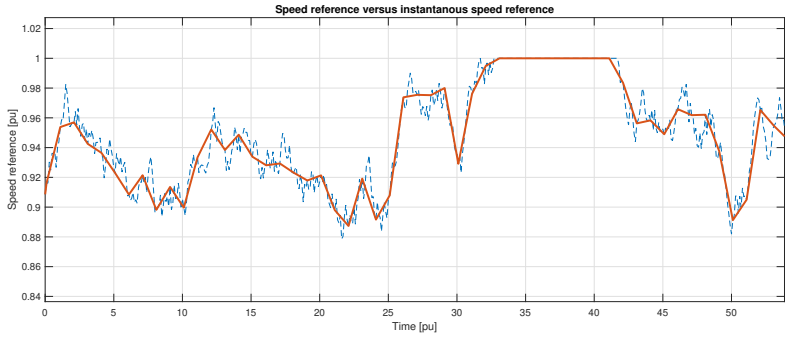

Figure 6.7: The speed reference given per second versus an ideal speed reference calculated for every 0.1 second. Time interval of 0 to 50 seconds from Figure 6.6.

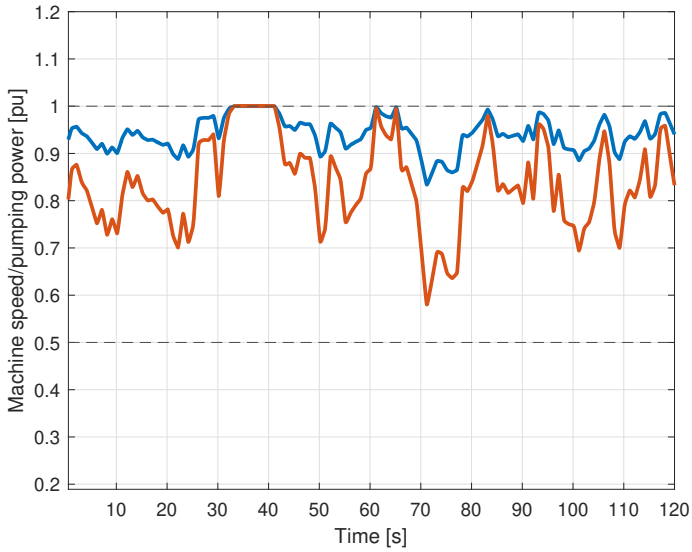

Figure 6.5: Per-unit values of the machine speed and pumping power for variable power output from the wind power source in Scenario A. Dotted horizontal lines represent the minimum and maximum power limits.

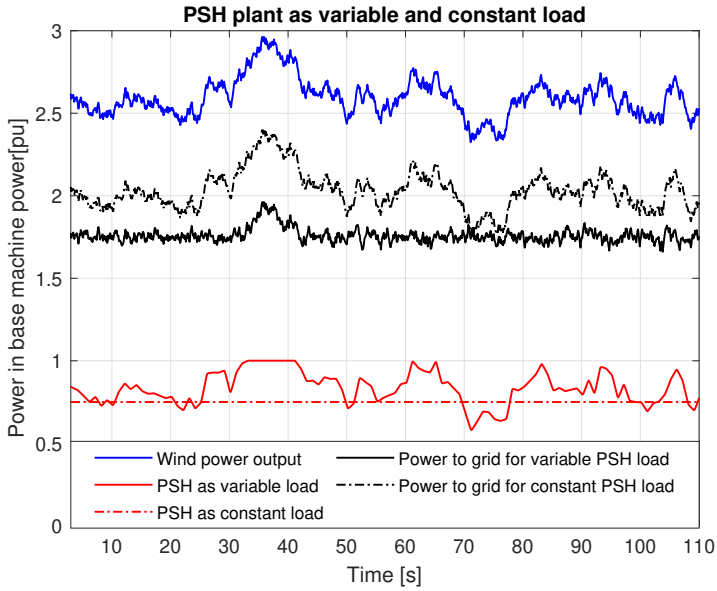

Figure 6.6: A comparison of using the PSH as a variable (*thick lines*) and constant (*dotted lines*) load, and how this affects the power flow to the external grid when generation is dominated by a variable wind power source (blue line).

6.3 Scenario B: Frequency Control of Pump Load

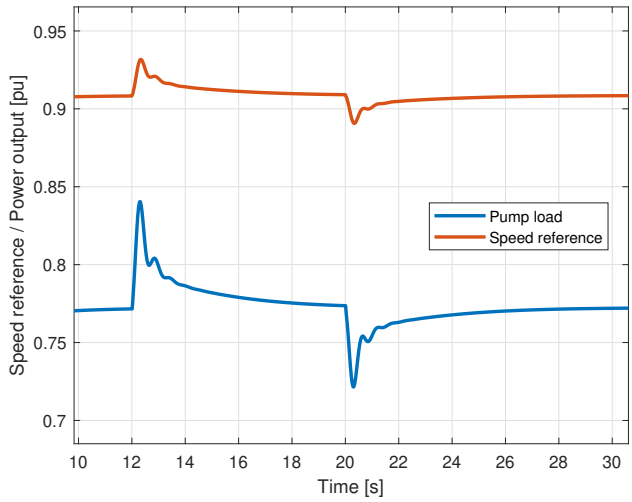

Figure 6.8: The variation of machine speed reference and pumping power during disconnection (*12 seconds*) and connection (*20 seconds*) of load.

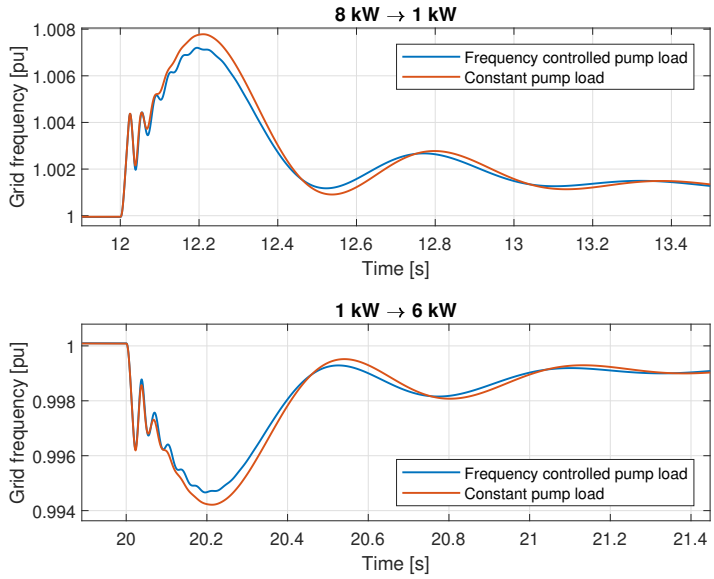

Figure 6.9: A comparison of the frequency response for a system with and without frequency-controlled pump load in Scenario B.

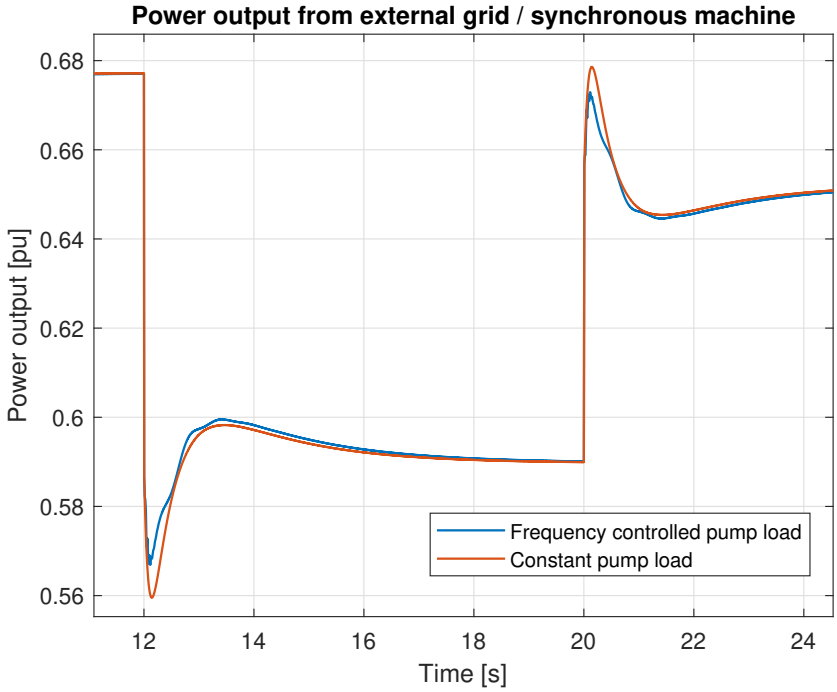

Figure 6.10: A comparison of power delivered from synchronous machine (*external grid*) for a system with and without frequency-controlled pump load in Scenario B.

6.4 Scenario C: Synthetic Inertia

Rotor Inertia Controller

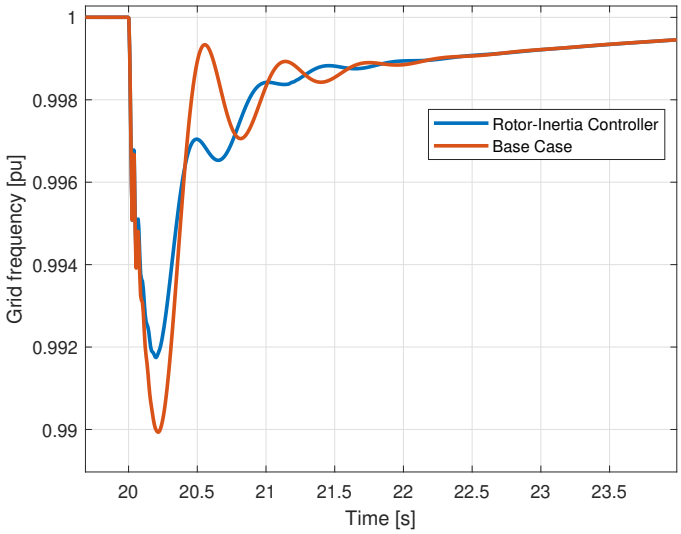

Figure 6.11: Comparison of frequency response after connection of a the 8 kW load.

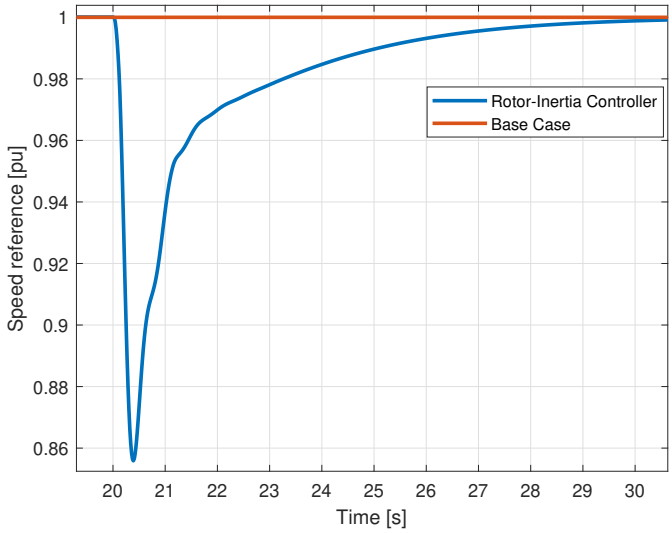

Figure 6.12: Speed reference given by rotor-inertia controller after connection of the 8 kW load.

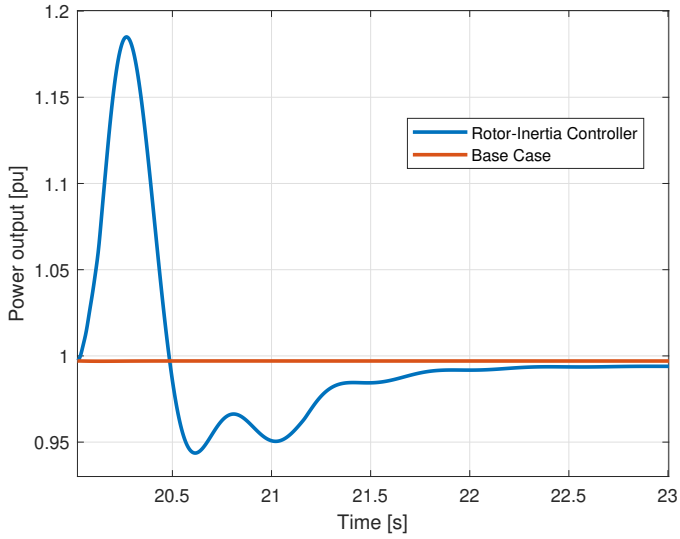

Figure 6.13: Power output for rotor-inertia controller.

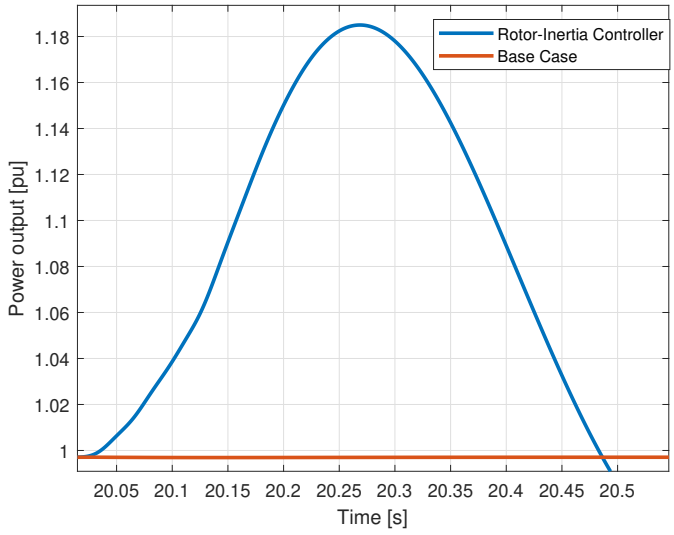

Figure 6.14: Close up of power boost from 20s to 20.5s.

Capacitor Inertia Controller

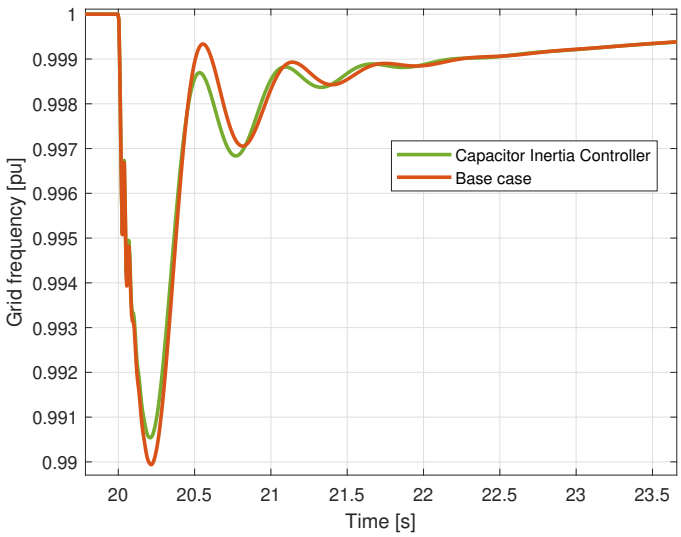

Figure 6.15: Comparison of frequency response after connection of the 8 kW load.

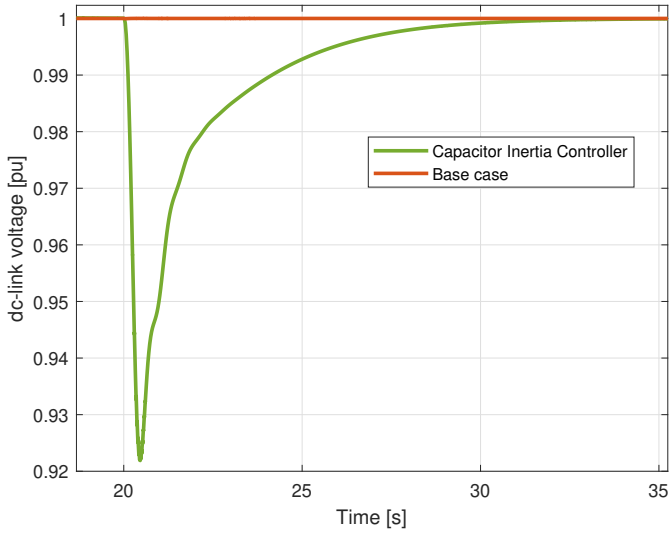

Figure 6.16: DC-link voltage after connection of the 8 kW load.

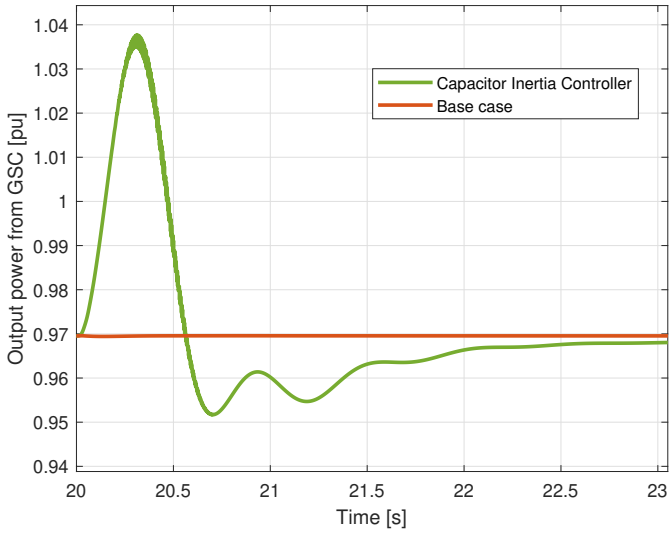

Figure 6.17: Power output for capacitor inertia controller.

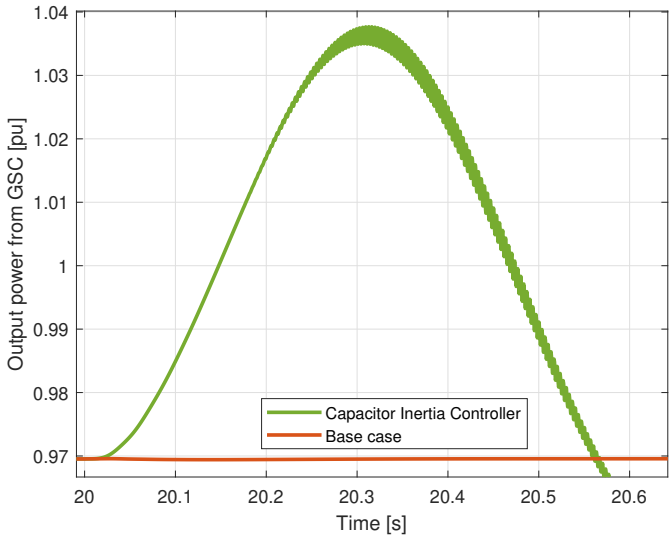

Figure 6.18: Close up of power boost.

Chapter 7

Discussion

7.1 Excitation System Control Strategy

Saturation Modelling

Table 6.1 presents the d-axis mutual inductances from the test case in Section 4.4. The differences between the approximated l_{ad} and the unsaturated value indicate the importance of modelling the effect saturation have on the mutual inductance. For the $\Psi_s = 1$ strategy, using the unsaturated value would have overestimated the mutual inductance by 3.9 %. Furthermore, l_{ad} is used in the calculation of the field current reference and would also affect this calculation. From Equation 4.5 it can be seen that for a converter-fed synchronous machine in steady-state operation where q-axis current and flux linkage is constant and the d-axis current is regulated to zero, the field current reference will be inversely proportional to the d-axis mutual inductance. Therefore, an overestimated d-axis mutual inductance will produce a too low field current reference, and consequently, the stator flux linkage will be regulated to a value lower than 1.0 pu. This means that less torque per ampere is obtained and that the full potential from the machine is not harvested.

It is observed that since d-axis current is regulated to zero by the converter, the d-axis mutual inductance depend solely on the field current according to Equation 4.6. This explains the difference between the approximated l_{ad} in Table 6.1 and the l_{ad} from the machine model in Figure 4.5, both for 1.0 pu field current. In Figure 4.5, the d-axis current will be non-zero such that the i_m is different for the two cases.

Field Current Control

From Table 6.2, it can be seen that by using higher field currents, the steady-state q-axis current will be reduced and a higher torque-per-ampere is achieved. It is observed that by using higher field currents, the ”available” q-axis current for a fast change in torque is higher, meaning that the converter can quickly produce a higher electrical torque when

the speed reference change. This is seen in Figure 6.1, by examining the differences in size between pre-load step q-axis current and the 1.0 pu ceiling of the different control strategies. For example: using a constant 1.0 pu field current, the q-axis current may only change with approximately 0.5 pu when the new speed reference is given. However, for a constant 2.0 pu field current, the q-axis current may change approximately 0.65 pu. The effect of this extra "available" q-axis current can be seen in Figure 6.3, where higher field currents lead to higher initial acceleration. The difference in the transition time from the initial speed to the reference speed is however small due to the current controller which reduces the q-axis current reference faster when a higher field current is used. This can be seen in Figure 6.1, where the q-axis current is held for longer time at 1 pu for the $i_{fd} = 1$ strategy, than the other strategies. The minor differences in acceleration time come as a consequence of the small size of the synchronous machine, thus the rotor inertia is quite small as well.

The mentioned higher initial acceleration when using higher field currents have one interesting characteristic and potential benefit when dealing with a load that is modelled as a centrifugal pump. In Figure 6.3, the higher field current strategies reach 0.90 pu speed and 0.95 pu speed faster than the $i_{fd} = 1.0$ pu strategy. For a centrifugal pump, the transition from 0.78 pu speed to 0.95 speed equals a 0.36 pu change in output power, or 72% of the applied load step. This means that by maintaining higher field currents, the PSH plant can ramp its power output faster than for lower field currents. While all strategies reach 1.0 pu power simultaneously, due to the current controller, this above-mentioned effect is beneficial during a loss of load event, when using the PSH plant as spinning reserve, since the greater share of the power step is brought online faster.

By using the $\Psi_s = 1$ strategy, the reference field current will change according to Equation 4.5, since the q-axis current changes both during and after the load step. It is seen from Figure 6.2, that only the $\Psi_s = 1$ strategy keeps the stator flux linkage constant, and that using the other strategies will result in a higher stator flux linkage after the load step. An objective of this analysis was to see how the control strategies affect the stator currents, field current and stator flux linkage. A higher stator current will naturally increase resistive losses in stator and the converter losses. However, this strategy may lead to higher field currents to produce the necessary stator flux linkage. If the stator flux linkage were to be regulated to values higher than its nominal value $\Psi_s > 1$, the machine will saturate and increase saturation related losses, but on the other hand, it will also lead to less current through the converter, reducing the converter losses.

7.2 Control Strategies for Variable Speed Hydropower

Scenario A: Power Control in Pump Mode

The effect of operating the PSH plant as a variable load, as opposed to a constant load, can be seen in Figure 6.6. By operating in variable speed and varying the pump load according to the power output of the wind power source, the PSH plant damps the power fluctuations observed by the grid towards a more constant flow of power. This is an indication of the

advantages variable speed PSH plants may provide to the power system, not only regular energy storage capacity, but to also perform load balancing services. With a variable speed PSH plant in the system, the wind power source may not need to be curtailed if it exceeds either power system demand or transmission line limitations. This means that more production capacity can stay online, thus increasing the reliability of the power system as well.

The ability to damp the power fluctuations of the wind power source is related to the rate of which the power set-point is updated, the acceleration of the machine-drive and the interval of power output for which the PSH may vary its load. The power variation capacity is determined by the allowable speed range of the reversible turbine. At these limits, the PSH plant is not able to provide more load balancing service, which can be seen in the test case from t = 30s to t = 40s where the upper power limit of the PSH is reached resulting in a higher than ordinary power variation observed by the grid.

If a shorter delay between each power reference calculation had been used, the PSH could have damped more of the variation in power seen by the black solid line in Figure 6.6. Figure 6.7 shows the speed reference sent to machine plotted with an ”ideal” speed reference calculated for every 0.1 seconds, i.e for each element of the Matlab vector containing the measured wind power. Using a more frequent update rate of the speed reference would have allowed the PSH plant to compensate more of the power fluctuations from the wind power generation. As stated earlier, this is however dependent on limitations of the mechanical system, such as if rapid speed changes are undesired or indeed impossible. As this model is a very small scale PSH plant, larger models will surely need longer delays between each new power set point. In [6], it is believed that the advantages of MW-sized variable speed PSH plants may lie in the scope of minutes or hours in terms of supporting the power system operation. Modern variable speed PSH plants could in this way smooth out the wind power variability at all times, not being confined to off-peak hours such as conventional PSH plants.

Scenario B: Frequency Control of Pump Load

Figure 6.8, shows how the pump load is varied by changing the speed reference to the machine-side converter controller. The load decrease and increase at t = 12 seconds and t = 20 seconds makes the PSH plant increase and decrease its pumping power respectively. The frequency-controlled pump load will change its pump load quickly according to the frequency deviation, before stabilizing when frequency is restored to 50 Hz.

Examining Figure 6.9, it can be seen that by operating the PSH plant as a frequency controlled load, the frequency response after a load change is improved slightly. For the load reduction from 8 kW to 1 kW, the increase in frequency is reduced by 12.5 %. For the load increase from 1 kw to 6 kW, the frequency drop is reduced by 8.6 %. As well a reducing frequency deviations, the frequency-controlled PSH plant reduces the variations in power output from the synchronous machine acting as an external grid, seen in Figure 6.10. A PSH plant acting as a frequency-controlled load can be able to reduce the ramping or start and stops of other generating units in the grid.

The frequency droop control contributes to maintaining the stability of the grid, and in [24] is its described as a contribution to the closed-loop control of the grid frequency. The load following control presented previously will also contribute to maintaining grid frequency, but it can be considered as a more direct way of controlling the influence of for example wind power. While both control strategies seek to balance generation and load, keeping the frequency constant, load following should be done at a much slower time scale than the frequency droop strategy. In a larger power system implementation, a PSH plant should make use of its fast response time and be used for fast frequency regulation, such that load following can be assigned to conventional power generation units. In a smaller system, a PSH plant could use a combination of these two strategies [28].

Scenario C: Synthetic Inertia

Figure 6.11 indicate that by releasing kinetic energy from the rotor, the initial drop in frequency can be slightly reduced. For the case with the rotor-inertia controller, the frequency drops to 0.9917 pu or 49.585 Hz, while it drops to 0.99 pu or 49.5 Hz for the base case. This is a 17% reduction in initial frequency drop by using the rotor inertia controller. The kinetic energy is released by quickly reducing the speed reference to 0.858 pu as seen in Figure 6.12. The effect of this speed reduction is that the power is boosted to a peak of 1.184 pu as shown in Figure 6.13-6.14. The effect of the rotor-inertia controller on the grid frequency seems to be rather limited, as the connected load is the same rating as the PSH ($8\ kW$). However, when the ratio between the sizes of the PSH plant and the load is more in favour of the PSH plant, the effect could perhaps become more pronounced. The tuning of the inertia controller constants was not the primary focus of this test case, but rather to show the principle of this controller.

The amount of energy supplied by this controller will be limited by the operating speed of the machine and the allowable speed deviations from this operating point. A limit of $\pm$ 25% were mentioned based on [7]. However, as variable speed units are allowed to operate at lower speeds, the available kinetic energy from the rotor may be less when operating at speeds below 1.0 pu. For larger units in the MW-scale it may also be a question if the rotor is allowed to reduce its speed as sharply as presented here, due to mechanical stress factors. Furthermore, the internal electronics of the frequency converter may also see increased degradation due to fast short-term increase in voltage and current. Therefore, a real-life application of such a rotor-inertia controller will need to take such constraints into account.

Similarly to the rotor inertia controller, power is quickly injected into the grid by reducing the dc-link voltage reference. However, the amount of power that can be supplied by the capacitor inertia controller is much smaller than for the rotor inertia controller. The capacitor inertia controller will deliver at a peak of 1.038 pu power. Based on Figure 6.14 and 6.18, it can be calculated that the rotor inertia controller is able to inject approximately 4.5 times more power in the first 0.5 seconds. The effect of this can be seen in Figure 6.11 and 6.15, where the reduction in frequency drop by using the capacitor inertia controller is lesser than for the rotor inertia controller. The differences can be explained by the unequal amount of energy stored in the rotor and the dc-link capacitor, and the limitations

in minimum allowable speed and dc-link voltage.

7.3 Simulation Model

The synchronous machine used in this CFSM system was based on a real-life NTNU laboratory generator which also had been treated in a previous master thesis. This meant that all parameters of the synchronous machine, including saturation curve, already had been found and analysed. When modelling the saturation effects in Section 4.2, having the saturation curve was the main reason for choosing this machine. However, later when control strategies for variable speed PSH plants were to be analysed in Chapter 5, the small size of the machine became apparent. Real-life PSH plants for larger power grid implementation would be in the MW-scale, with significantly slower dynamics as was seen from the 8 kVA synchronous machine used in this thesis. With a larger machine, the results from Figure 6.3 could perhaps have been more visible, indicating that by using higher field currents the acceleration would be increased. By using a large MW-scale synchronous machine from the start, the parameter data would have to be taken from typical per-unit values as reference machine in the MW-scale was not to be found. Per-unit values are generally the same for most synchronous machines with a given power rating, and would likely give reasonable results for the simulations in Simulink.

Furthermore, the overall control system of the CFSM was based on classical torque control where the machine-side converter controls the speed, governor controls power and grid-side converter controls the dc-link voltage. This is a well-proven technique that provided a satisfactory behaviour of the developed model. However, more advanced controllers could be implemented as well, such as the *Virtual Synchronous Machine* type of control. Here, the machine-side converter controls the dc-link voltage, the governor controls the speed and the grid-side converter controls active and reactive power. Such type of control was employed in both [4] and [29], enabling very fast power injection to the grid. The presented model could for further work be expanded to include such type of control, especially in generator mode where fast speed changes are less important in the short-term focus.

Finally, while the controllability of the CFSM is high, it will be constrained by the operational limits of the hydraulic system. For some of the test scenarios, speed limitations were taken from literature and real-life examples; However, other constraints related to water hammering, pressure and mass oscillations were not taken into account directly. Further work could include delving into how the constraints of the hydraulic system will affect the operation of the CFSM, as this will be key to formulating good, real-life control strategies. In addition to abiding the constraints, optimization of the control strategy should also include optimizing hydraulic efficiency, minimize losses in the hydraulic and electric system, and minimize the operation of the guide vane servo. When these constraints and internal plant objectives are known, the real grid-support capabilities of the CFSM will be more visible.

Chapter 8

Conclusion

During the course of this thesis, a simulation model of a pumped-storage plant was developed in Simulink, containing models for both pump mode and turbine mode. The parameters of the model were based on an 8 kVA synchronous machine, previously treated in [2]. The back-to-back VSCs were controlled according to a common procedure for wind power CFSMs [15]. The turbine parameters were extracted from available products online [14]. The control of the excitation system for a converter-fed synchronous machine has more degrees of freedom than conventional direct grid-connected synchronous machines. Since the grid-voltage can be supported by the grid-side converter, the excitation system does not need to take part in AVR action. In this thesis, it was shown that by controlling the stator flux linkage amplitude to 1.0 pu, a better torque-per-ampere rate could be achieved with the machine. Both pump mode and generating mode of the variable speed PSH plant was simulated in Simulink. By using the PSH plant as a load following or frequency-controlled plant, the operation and reliability of the power grid is improved. The last scenario examined the use of inertia controllers for emulating inertia of the CFSM. An inertia controller for both the kinetic energy stored in the rotor and in the dc-link capacitor was developed, and they both proved to be able to provide the grid with fast power injections during frequency disturbances.

Further work of this thesis should include implementation of an improved control strategy, especially for generation mode where fast speed changes are less important and the mechanical speed could be controlled by the governor thereby freeing the machine-side converter from the responsibility of speed regulation. The VSM strategy presented in [4] looks promising, enabling fast power injections, also without supplementary inertia controllers. Furthermore, the excitation system control is another area of this thesis that could be expanded upon: more accurate modelling of the excitation system, improving the control strategy, and more in-depth saturation modelling are examples. Finally, the presented model should be implemented with a larger machine in the MW-scale such that more realistic scenarios regarding the grid integration of pumped-storage plants can be created.

Bibliography

[1] "Advantages of variable speed pump turbines for adjusting power supply," September 2011. Mitsubishi Heavy Industries Technical Review Vol. 48 No. 3.

[2] E. H. Bjørkhaug, "Adjustable speed of synchronous machine for hydro power application," 2017. [Master Thesis NTNU].

[3] "Teknisk ukeblad 21.mai 2020." https://www.tu.no/artikler/boston-professor-allvar-forskning-tilsier-at-det-i-ikke-i-blir-veldig-utbredt-a-koble-seg-av-stromnettet/492520. [Online; accessed 03-06-2020].

[4] T. I. Reigstad and K. Uhlen, "Variable speed hydropower conversion and control," *IEEE Transactions on Energy Conversion*, vol. 35, no. 1, pp. 386–393, 2020.

[5] M. Valavi and A. Nysveen, "Variable-speed operation of hydropower plants: A look at the past, present, and future," *IEEE Industry Applications Magazine*, vol. 24, pp. 18–27, Sep. 2018.

[6] MWH, "Technical analysis of pumped storage and integration with wind power in the pacific northwest." https://www.hydro.org/wp-content/uploads/2017/08/PS-Wind-Integration-Final-Report-without-Exhibits-MWH-3.pdf, 2009. [Online; accessed 08-05-2020].

[7] I. Iliev, C. Trivedi, and O. Dahlhaug, "Variable-speed operation of francis turbines: A review of the perspectives and challenges," *Renewable and Sustainable Energy Reviews*, vol. 103, pp. 109–121, 04 2019.

[8] T. Beyer, "Goldisthal pumped-storage plant: more than power production." https://www.hydroreview.com/2007/03/01/goldisthal-pumped-storage-plant-more-than-power-production/#gref, 03.01.2007. [Online; accessed 11-05-2020].

[9] R. J. Kerkman, T. A. Lipo, W. G. Newman, and J. E. Thirkell, "An inquiry into adjustable speed operation of a pumped hydro plant part 1 - machine design and performance," *IEEE Transactions on Power Apparatus and Systems*, vol. PAS-99, pp. 1828–1837, Sep. 1980.

[10] P. K. Steimer, O. Senturk, S. Aubert, and S. Linder, "Converter-fed synchronous machine for pumped hydro storage plants," in *2014 IEEE Energy Conversion Congress and Exposition (ECCE)*, pp. 4561–4567, Sep. 2014.

[11] The Mathworks, Inc., Natick, Massachusetts, *MATLAB version R2019b*, 2019.

[12] T. K. Nielsen, "Simulation model for francis and reversible pump turbines," 2015.

[13] P. Kundur, "Power system stability and control," 1994. [Online; accessed 14-04-2020].

[14] "8kw francis turbine." https://willgainpower.en.made-in-china.com/product/SedmolHMSwUb/China-8kw-Francis-Type-Hydro-Turbine-System.html. [Online; accessed 18-05-2020].

[15] L. Quéval and H. Ohsaki, "Back-to-back converter design and control for synchronous generator-based wind turbines," in *2012 International Conference on Renewable Energy Research and Applications (ICRERA)*, pp. 1–6, Nov 2012.

[16] R. Nilsen, "Elektriske motordrifter, synkronmotordrifter."

[17] I. S. University, "Representation of saturation in stability studies." http://home.engineering.iastate.edu/~jdm/ee554/saturation.pdf. [Online; accessed 14-04-2020].

[18] Mathworks, "Salient-pole synchronous machine." https://se.mathworks.com/help/physmod/sps/ref/synchronousmachinesalientpole.html. [Online; accessed 14-04-2020].

[19] Mathworks, "Model the dynamics of three-phase round-rotor or salient-pole synchronous machine." https://se.mathworks.com/help/physmod/sps/powersys/ref/synchronousmachine.html. [Online; accessed 14-04-2020].

[20] O. Pyrhönen, "Analysis and control of excitation, field weakening and stability in direct torque controlled electrically excited synchronous motor drives," 1998.

[21] "Curve fitting toolbox." https://se.mathworks.com/products/curvefitting.html. [Online; accessed 14-04-2020].

[22] E. S. News, "'world's tallest' wind turbine gets 70mwh of pumped storage near stuttgart." https://www.energy-storage.news/news/worlds-tallest-wind-turbine-gets-70mwh-of-pumped-storage-near-stuttgart. [Online; accessed 07-05-2020].

[23] "Ge renewables - pumped-storage solutions." https://www.ge.com/renewableenergy/hydro-power/hydro-pumped-storage. [Online; accessed 07-05-2020].

[24] J. A. Suul, "Variable speed pumped storage hydropower plants for integration of wind power in isolated power systems," in *Renewable Energy* (T. J. Hammons, ed.), ch. 27, Rijeka: IntechOpen, 2009.

[25] T. Kuwabara, A. Shibuya, H. Furuta, E. Kita, and K. Mitsuhashi, "Design and dynamic response characteristics of 400 mw adjustable speed pumped storage unit for ohkawachi power station," *IEEE Transactions on Energy Conversion*, vol. 11, no. 2, pp. 376–384, 1996.

[26] J. Sarasúa, G. Martinez de Lucas, C. Platero, and J. Sanchez, "Dual frequency regulation in pumping mode in a wind–hydro isolated system," *Energies*, vol. 11, p. 2865, 10 2018.

[27] P. Vela, C. Valenzuela, and J. Espinoza, "Using the dc-link capacitor as a rotating inertia in a three phase pv system," in *2017 IEEE XXIV International Conference on Electronics, Electrical Engineering and Computing (INTERCON)*, pp. 1–4, 2017.

[28] J. A. Suul, K. Uhlen, and T. Undeland, "Wind power integration in isolated grids enabled by variable speed pumped storage hydropower plant," in *2008 IEEE International Conference on Sustainable Energy Technologies*, pp. 399–404, 2008.

[29] M. Gallefoss, "Synthetic inertia from a converter-fed synchronous machine in a hydro-electric power plant," 2018. [Master Thesis NTNU].

Appendix

A Salient Pole Synchronous Machine Equations

The full per-unit model of the salient pole synchronous machine is given by equations 8.1-8.6 [16]:

$$v_d = r_s \cdot i_d + \frac{1}{\omega_n}\frac{d\psi_d}{dt} - n \cdot \psi_q \tag{8.1}$$

$$v_q = r_s \cdot i_q + \frac{1}{\omega_n}\frac{d\psi_q}{dt} + n \cdot \psi_d \tag{8.2}$$

$$v_0 = r_s \cdot i_0 + \frac{1}{\omega_n}\frac{d\psi_0}{dt} \tag{8.3}$$

$$v_f = r_f \cdot i_0 + \frac{1}{\omega_n}\frac{d\psi_f}{dt} \tag{8.4}$$

$$0 = r_D \cdot i_D + \frac{1}{\omega_n}\frac{d\psi_D}{dt} \tag{8.5}$$

$$0 = r_Q \cdot i_Q + \frac{1}{\omega_n}\frac{d\psi_Q}{dt} \tag{8.6}$$

Where the flux linkage are defined as:

$$\psi_d = x_d \cdot i_d + x_{ad} \cdot i_f + x_{ad} \cdot i_D \tag{8.7}$$

$$\psi_q = x_q \cdot i_q + x_{aq} \cdot i_Q \tag{8.8}$$

$$\psi_0 = x_l \cdot i_0 \tag{8.9}$$

$$\psi_f = x_{ad} \cdot i_d + x_f \cdot i_f + x_{ad} \cdot i_D \tag{8.10}$$

$$\psi_D = x_{ad} \cdot i_d + x_{ad} \cdot i_f + x_D \cdot i_D \tag{8.11}$$

$$\psi_Q = x_{aq} \cdot i_q + x_Q \cdot i_Q \tag{8.12}$$

The per-unit reactances as:

$$x_d = x_l + x_{ad} \tag{8.13}$$

$$x_q = x_l + x_{aq} \tag{8.14}$$

$$x_f = x_{fl} + x_{ad} \tag{8.15}$$

$$x_D = x_{ad} + x_{Dl} \tag{8.16}$$

$$x_Q = x_{aq} + x_{Ql} \tag{8.17}$$

The electrical torque and acceleration is given as:

$$T_e = \psi_d \cdot i_q - \psi_q \cdot i_d \tag{8.18}$$

$$t_m \frac{dn}{dt} = T_e - T_l \tag{8.19}$$

$$\frac{d\theta}{dt} = \omega_n \cdot n \tag{8.20}$$

Steady-state equations:

By neglecting damper windings, the equations can in steady-state be reduced to:

$$v_d = r_s \cdot i_d - n \cdot \psi_q \tag{8.21}$$

$$v_q = r_s \cdot i_q + n \cdot \psi_d \tag{8.22}$$

$$v_f = r_f \cdot i_f \tag{8.23}$$

$$\psi_d = x_d \cdot i_d + x_{ad} \cdot i_f \tag{8.24}$$

$$\psi_q = x_q \cdot i_q \tag{8.25}$$

$$T_e = \psi_d \cdot i_q - \psi_q \cdot i_d \tag{8.26}$$

Entering the expressions for the flux linkages from equations 8.7-8.12, we obtain:

$$v_d = r_s \cdot i_d - n \cdot x_q \cdot i_q \tag{8.27}$$

$$v_q = r_s \cdot i_q + n \cdot x_d \cdot i_d + n \cdot x_{ad} \cdot i_f \tag{8.28}$$

$$T_e = x_{ad} \cdot i_f \cdot i_q + (x_d - x_q) \cdot i_d \cdot i_q \tag{8.29}$$

B System Modelling in Simulink

B.1 System Parameters

Table 8.1: Parameter values for the salient-pole synchronous machine. All system parameters are viewed from the stator.

Symbols	Name	Value
S_n	Nominal apparent power	8 kVA
V_n	Nominal line-to-line voltage (rms)	220 V
I_n	Nominal current	21 A
f_n	Nominal frequency	50 Hz
P	Number of pole pairs	3
R_s	Stator resistance (pu)	0.0361
X_l	Stator leakage reactance (pu)	0.0644
X_d	d-axis reactance (pu)	0.644
$X_d^{'}$	d-axis transient reactance (pu)	0.218
$X_d^{''}$	d-axis sub-transient reactance (pu)	0.083
X_q	q-axis reactance (pu)	0.423
$X_q^{''}$	q-axis sub-transient reactance (pu)	0.423
$T_d^{'}$	d-axis short-circuit transient time constant	0.069 s
$T_d^{''}$	d-axis short-circuit sub-transient time constant	0.0062 s
$T_q^{''}$	q-axis short-circuit sub-transient time constant	0.0062 s

Table 8.2: Mechanical Parameters of the Synchronous Machine.

Symbol	Name	Value
J	Total inertia	0.3 $kg \cdot m^2$
T_m	Mechanical time constant	0.41 s
H	Inertia time constant	0.205 s

Table 8.3: Excitation System Parameters.

Symbol	Name	Value
E_{fd}	Nominal field voltage	112 V
I_{fd}	Nominal field current	2.6 A
$T_{fd,i}$	Field current measurement time constant	2 ms
R_{fd}	Field circuit resistance	0.012 pu
X_{fd}	Field circuit reactance	0.21 pu

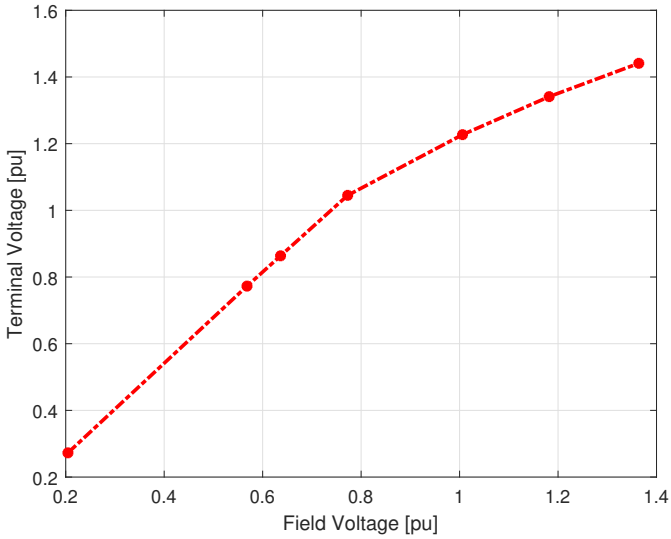

Figure 8.1: The per-unit saturation curve of synchronous machine [2].

Table 8.4: Hydraulic Turbine and Governor Parameters.

Symbol	Name	Value
T_w	Water starting time	0.1 s*
Q_r	Design flow rate	0.17 m^3/s*
H_r	Design head	6.4 m*
g_{fl}	Gate opening at full-load	0.94 pu
g_{nl}	Gate opening at no-load	0.06 pu
g_{fl}	Gate opening at full-load	0.94
T_p	Pilot valve and servomotor time constant	0.05 s
K_s	Servo gain	20
A_t	Turbine gain	1.136
T_g	Main servo time constant	0.2 s
R_p	Permanent droop	0.04 s
$R_{max,open}$	Maximum gate opening rate	0.16 pu/s
$R_{max,close}$	Maximum gate closing rate	- 0.16 pu/s
g_{max}	Maximum gate position	1
g_{min}	Minimum gate position	0

*NOTE: Turbine data marked with * is extracted from commercially available small-scale Francis turbine [14]. The rest are typical per-unit quantities of hydropower units given in Prabha Kundur's Power System Stability and Control [13].*

Table 8.5: Converters and DC-link Parameters.

Symbol	Name	Value
S_n	Nominal converter power	10 kVA
V_{dc}	Nominal DC-link voltage	600 V
f_{sw}	Converter switching frequency	4000 Hz
C_{dc}	DC-link capacitor	6.6 mF

Table 8.6: Grid and LCL-filter Parameters.

Symbol	Name	Value
V_{ac}	Nominal grid voltage (LL,rms)	400 V
L_{grid}	Line inductance	600 μH
R_{grid}	Line resistance	10 mΩ
L_{LCL}	Inductance of LCL-filter	1 mH
C_{LCL}	Capacitance of LCL-filter	25 μF
R_{LCL}	Resistance of LCL-filter	20 mΩ

B.2 System Base Values

Machine Base Values

The nominal apparent power is used as the base power, while the nominal stator phase voltage (peak-value) is used as base voltage. Choosing the base values as the peak of their sinusoidal function has benefits for the control system, which in real life are measured, sampled and transferred to dq-quantities [2]. From these quantities, the following base values are calculated:

Table 8.7: Machine Base Values.

Symbol	Name	Value
S_b	Base power	8 kVA
V_b	Base voltage	179.6 V
I_b	Base current	29.7 A
Z_b	Base impedance	6.05 Ω
$w_{el,b}$	Base electrical speed	100π rad/s
L_b	Base inductance	0.0193 H
$w_{m,b}$	Base mechanical speed	104.7 rad/s
t_b	Base torque	76.4 Nm

DC-link Base Values

The converter is rated 10 kVA, and the nominal DC-link voltage is set to 600 V. The base values of the DC-link is then calculated as:

$$I_{dc,base} = \frac{S_{dc}}{V_{dc}} = \frac{10000VA}{600V} = 16.7A$$

$$Z_{dc,base} = \frac{V_{dc}}{I_{dc}} = \frac{600V}{16.7A} = 35.9\Omega$$

Grid Base Values

As the grid is represented by an ideal voltage source, the rating of the converter is used as the base power. Nominal grid voltage is 400 V (LL,rms). Then, the base values of the grid side is calculated as:

$$V_b = \frac{V_{grid,peak}}{\sqrt{3}} = \frac{\sqrt{2} \cdot V_{ac}}{\sqrt{3}} = 326.6V$$

$$I_b = \sqrt{\frac{2}{3}} \cdot \frac{S_{ac}}{V_{ac}} = \frac{\sqrt{2} \cdot 10000VA}{\sqrt{3} \cdot 400V} = 23.6A$$

$$Z_b = \frac{V_b}{I_b} = \frac{326.6V}{23.6A} = 13.8\Omega$$

$$L_b = \frac{Z_b}{\omega_{grid}} = \frac{13.8\Omega}{2 \cdot \pi \cdot 50Hz} = 0.0441H$$

B.3 Controller Parameters

The inner current control loops are tuned according to modulus optimum while the outer speed and DC-link voltage control loops of the machine-side and grid-side converter respectively are tuned according to symmetrical optimum. The following controller gains are applied for the PI-regulators:

Table 8.8: Machine-side converter controller parameters.

Symbol	Name	Value
K_{pd}	Proportional gain, d-axis current controller	0.9612
K_{id}	Integral gain, q-axis current controller	133.8
K_{pq}	Proportional gain, d-axis current controller	1.2014
K_{iq}	Integral gain, q-axis current controller	74.68
K_{ps}	Proportional gain, speed controller	63.9201
K_{is}	Integral gain, speed controller	2879.3

Table 8.9: Grid-side converter controller parameters.

Symbol	Name	Value
K_{pd}	Proportional gain, d-axis current controller	0.2222
K_{id}	Integral gain, q-axis current controller	18.02
K_{pq}	Proportional gain, d-axis current controller	0.2222
K_{iq}	Integral gain, q-axis current controller	18.0225
K_{ps}	Proportional gain, voltage controller	68.07
K_{is}	Integral gain, voltage controller	4875

The field current controller uses the resistance and inductance values obtained from a previous master thesis [2] given in Table 8.3. First, the merged time constant T_{sum} is calculated as $T_{sum} = T_{fd,i} + T_{delay}$. Since real excitation system relies on a converter, there will be a delay related to this component. In this thesis it is assumed equal to T_{sw} of the grid- and machine-side converters.

$$T_{sum} = T_{f,i} + T_{delay} = 0.2ms + 0.25ms = 0.45ms$$

$$k_{pf} = \frac{\frac{X_{fd}}{\omega}}{2 \cdot T_{sum}} = \frac{\frac{0.21}{100\pi}}{2 \cdot 0.45 \cdot 10^{-3}} = 0.743$$

$$T_{i,f} = \frac{X_{fd}}{\omega \cdot (R_{fd} + 0.9 \cdot R_a)} = 0.015s$$

$$k_{if} = \frac{k_{pf}}{T_{i,f}} = \frac{0.743}{0.015} = 49.5$$

B.4 System Implementation

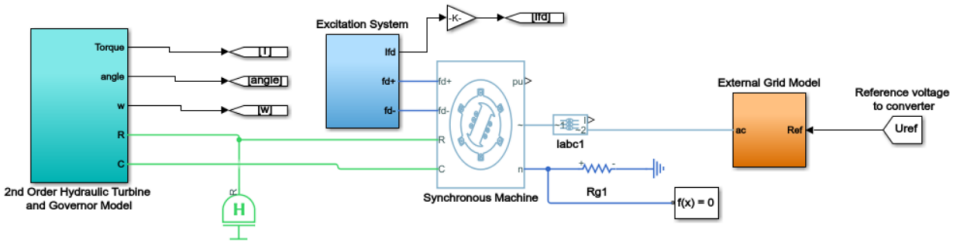

Figure 8.2: Overview of general CFSM system.

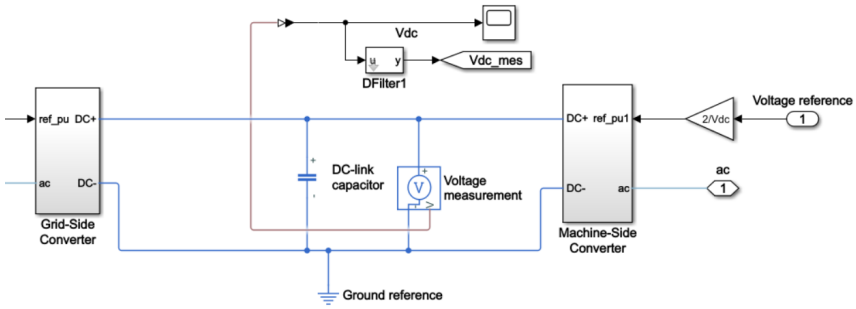

Figure 8.3: Back-to-Back Converter and dc-link.

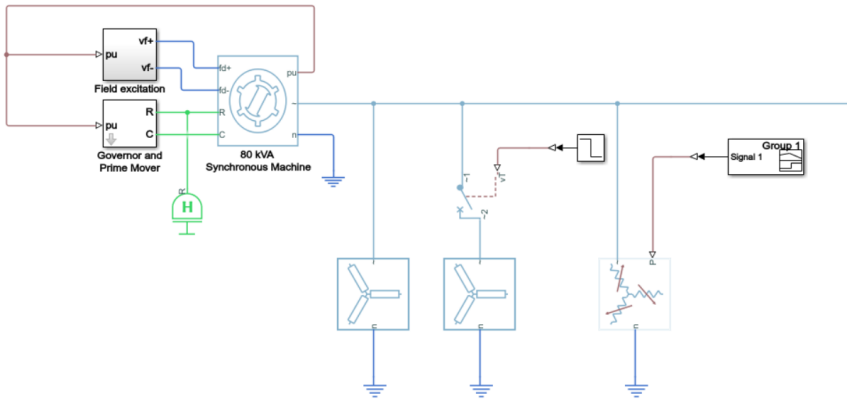

Figure 8.4: External grid represented by a 80 kVA synchronous machine.

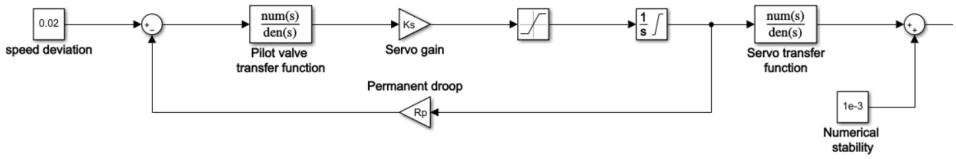

Figure 8.5: Governor.

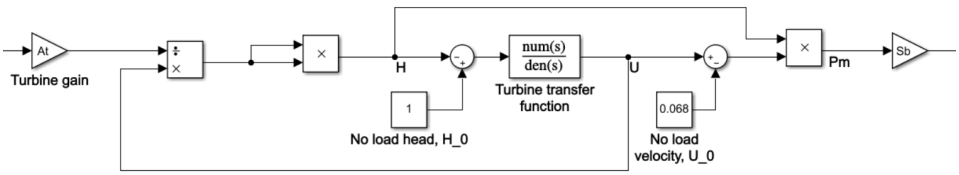

Figure 8.6: Turbine.

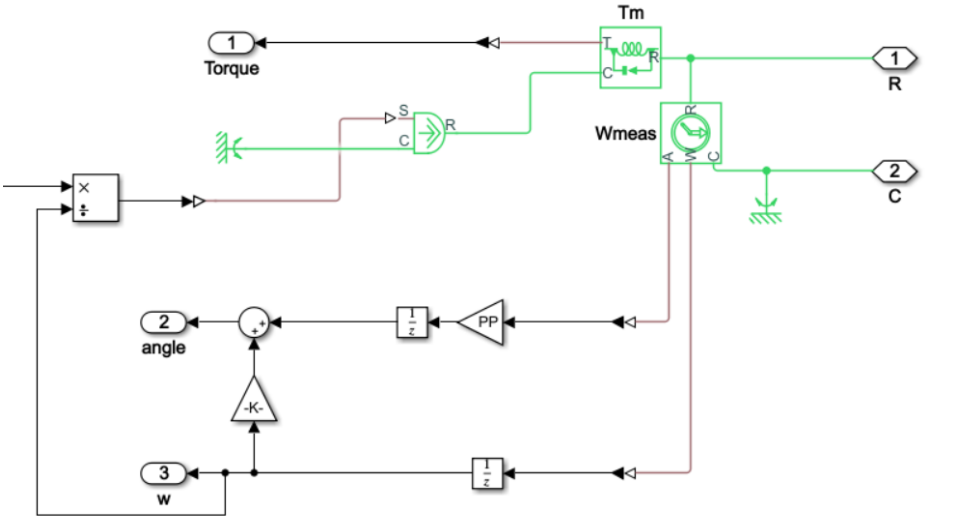

Figure 8.7: Conversion of turbine simulink signal to physical signal.

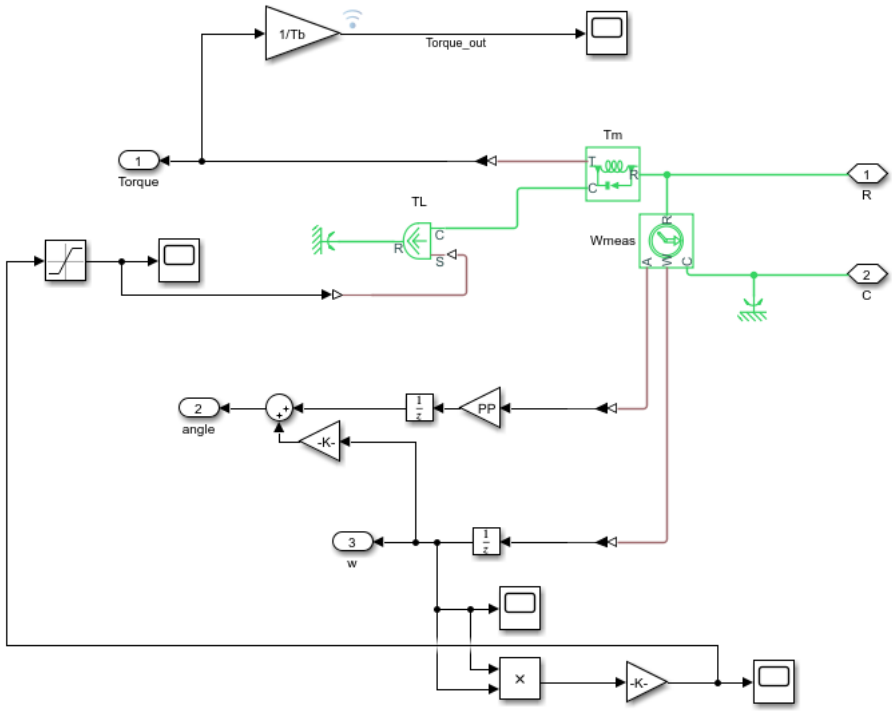

Figure 8.8: Centrifugal pump model in Simulink.

Machine-Side Converter

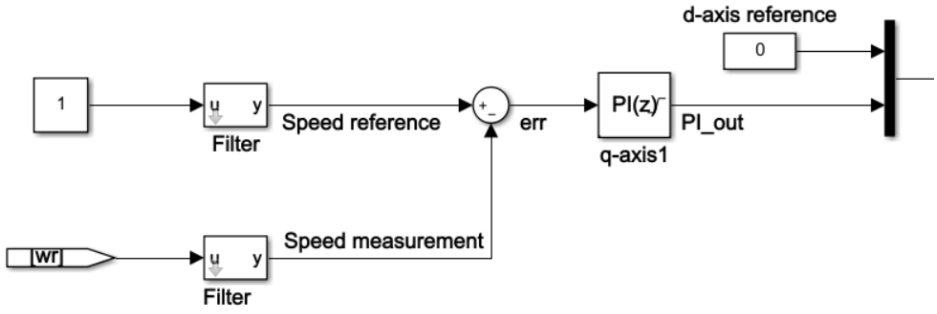

Figure 8.9: Outer control loop of the machine-side converter, part 1.

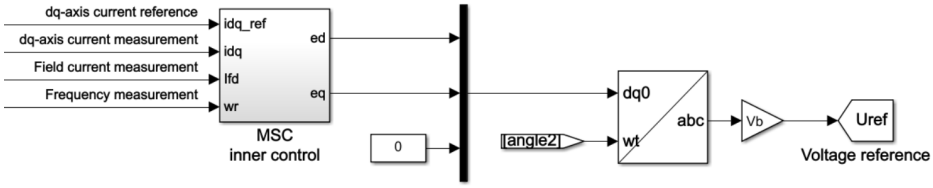

Figure 8.10: Outer control loop of the machine-side converter, part 2.

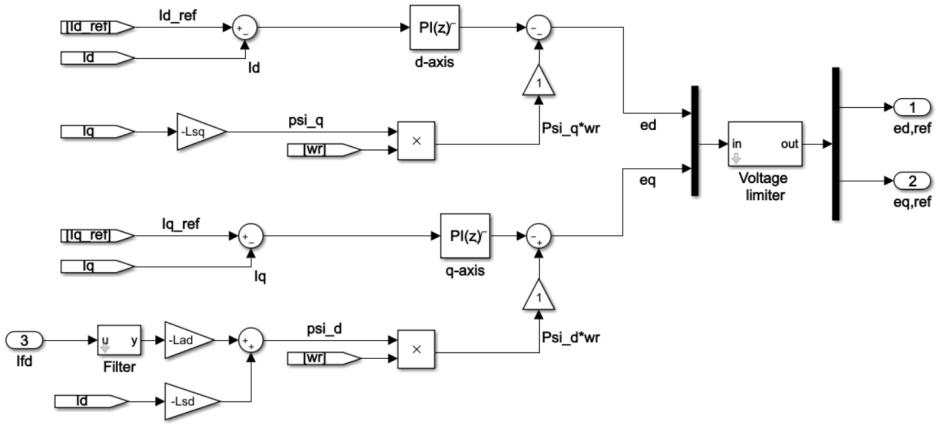

Figure 8.11: Inner control loop of the machine-side converter.

Grid-Side Converter

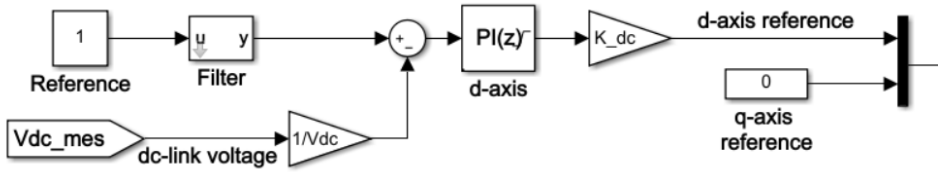

Figure 8.12: Outer control loop of the grid-side converter, part 1.

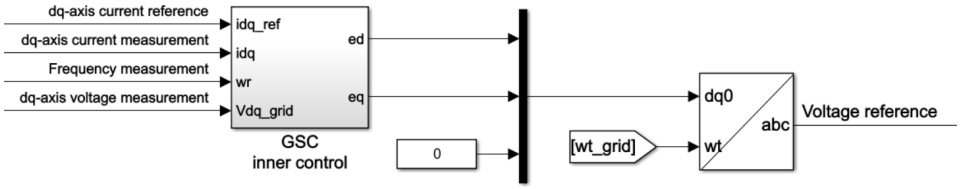

Figure 8.13: Outer control loop of the grid-side converter, part 2.

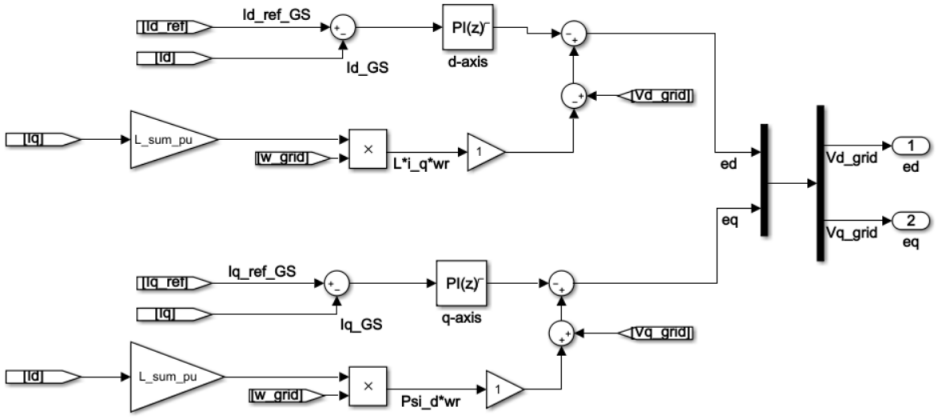

Figure 8.14: Inner control loop of the grid-side converter.

C Excitation System Control

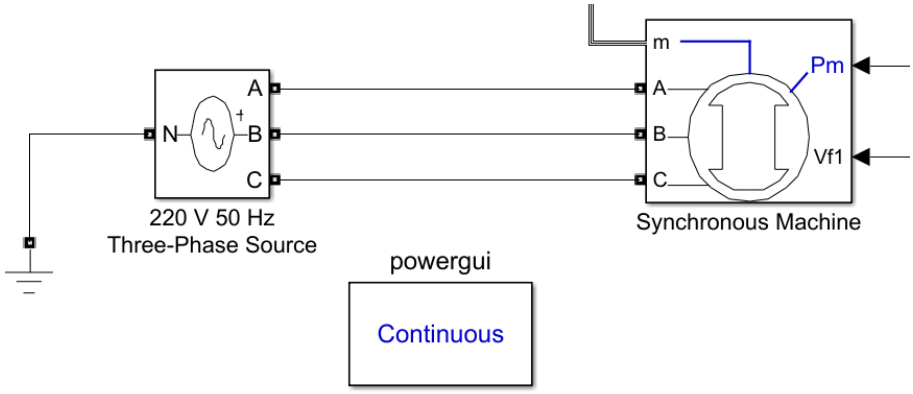

Figure 8.15: The Simulink model used for modelling of saturation.

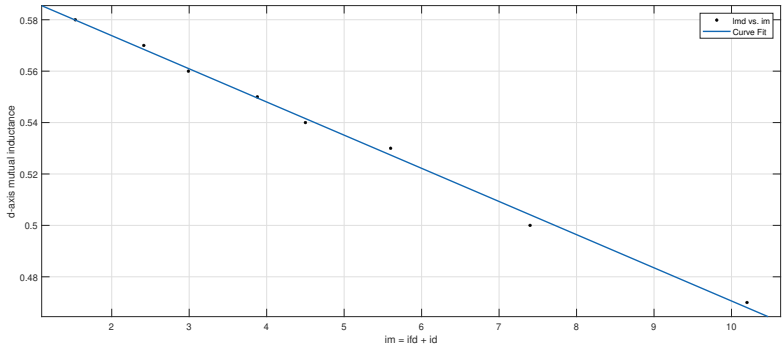

Figure 8.16: The curve fitted to the data-points of l_{ad} for varying magnetization.

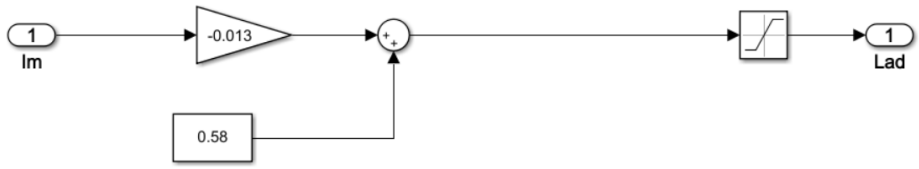

Figure 8.17: Implementation of Equation 4.6 in Simulink.

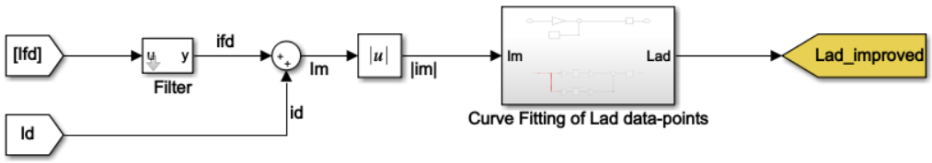

Figure 8.18: Approximation of l_{ad}.

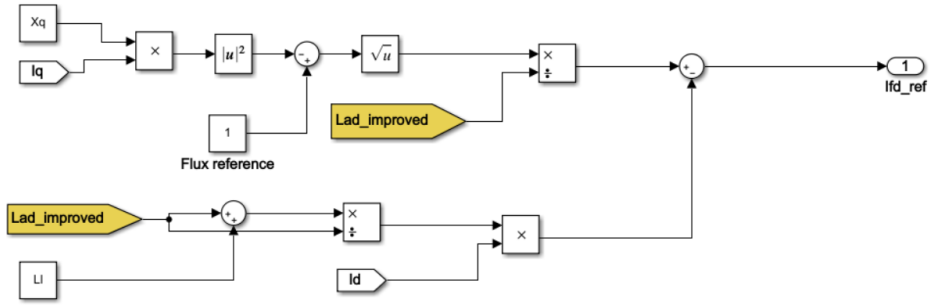

Figure 8.19: Ψ_s-controller.

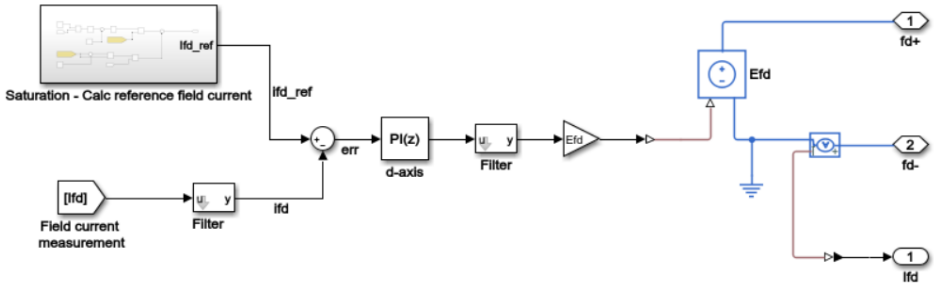

Figure 8.20: Excitation system.

D Frequency Control of Pump Power

D.1 Frequency Droop Characteristic

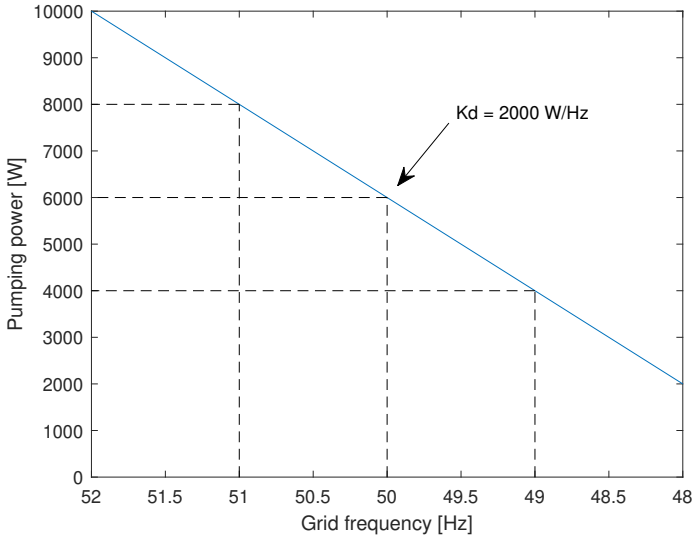

Figure 8.21: The frequency droop curve of the PSH plant.

D.2 Frequency Droop Controller in Simulink

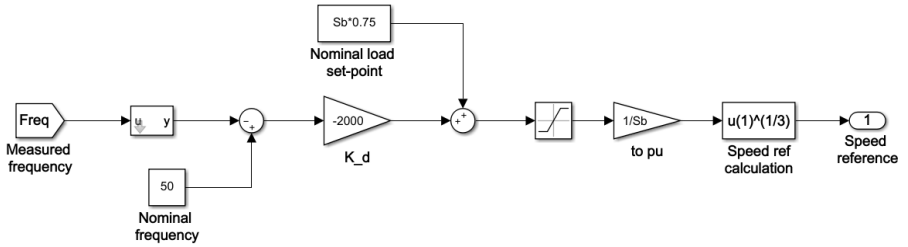

Figure 8.22: Implementation of frequency control of the pumping power.

D.3 Test Case: Frequency Controlled Pump Load

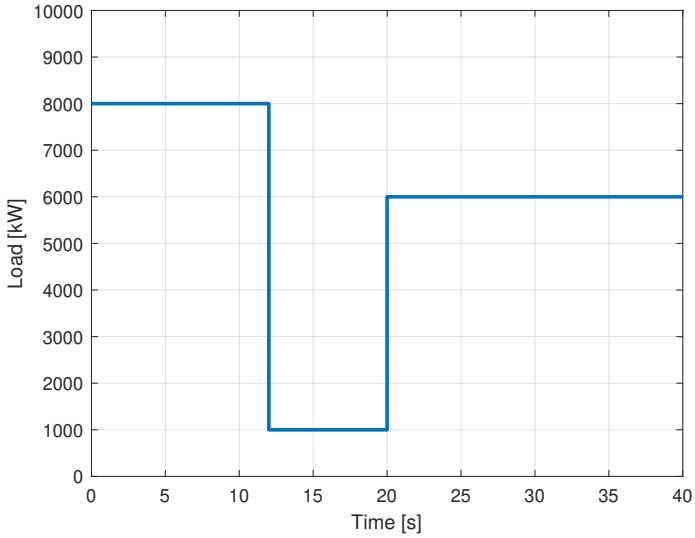

Figure 8.23: Power consumed by the variable load in the test case.

D.4 Synchronous Machine as External Grid

Table 8.10: Parameter values of the external grid represented by a synchronous machine.

Symbols	Name	Value
S_n	Nominal apparent power	80 kVA
V_n	Nominal line-to-line voltage (rms)	400 V
PP	Pole pairs	2
H	Inertia constant	1 s
f	Nominal frequency	50 Hz
I_{field}	Field current to produce nominal voltage	100 A
$L_{ad,unsat}$	Unsaturated d-axis mutual inductance	1.66 pu
$L_{aq,unsat}$	Unsaturated q-axis mutual inductance	1.61 pu
L_l	Stator leakage inductance	0.015 pu
R_a	Stator resistance	0.003 pu
L_{fd}	Rotor field circuit inductance	0.165 pu
R_{fd}	Rotor field circuit resistance	0.0006 pu
L_{1d}	d-axis damper winding inductance	0.1713 pu
R_{1d}	d-axis damper winding resistance	0.0284 pu
L_{1q}	q-axis damper winding inductance	0.1066 pu
R_{1q}	q-axis damper winding resistance	0.0650 pu

Table 8.11: AC-side loads. All loads were purely resistive.

Name	Value
Constant load	40 kW
Connectable load	8 kW

E Rotor Inertia Controller

The rotor inertia controller seen in Figure 5.5 contains two parts: a derivative controller and a droop controller. Separately, the inertia controllers will give the speed references seen in Figure 8.24. The resulting power response can be seen in Figure 8.25. The derivative controller will quickly reduce the speed reference, but also quickly increase as the frequency goes from dropping to increasing back to 50 Hz. This causes the power output of the machine to fluctuate, thus not giving the lengthy power boost that is desired. The derivative controller was implemented with a logic that removes the second half of the speed reference seen in Figure 8.24. When the frequency drops, the speed reference above 0 is removed, and when the frequency increases the speed reference below 0 is removed. Furthermore, the sharp rise in speed reference from the derivative controller can be compensated for by a droop controller, right graph in Figure 8.24-8.25.

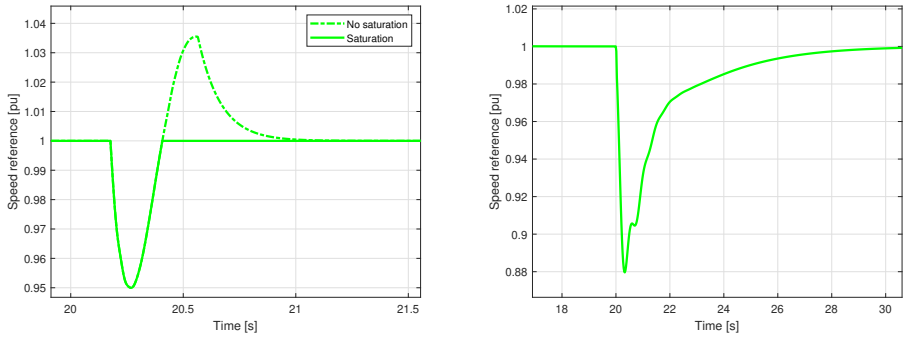

Figure 8.24: Left: Pure derivative controller with and without removal of positive speed reference. Right: Pure droop controller.

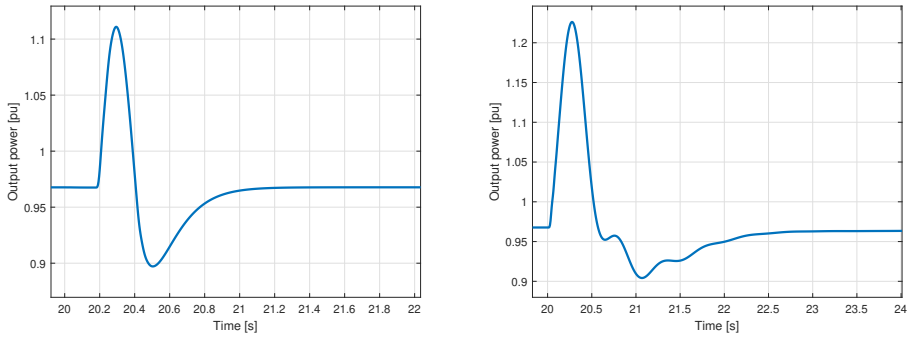

Figure 8.25: Power output seen from the grid-side converter. Left: Derivative controller Right: Droop controller.

A dead band from 49.9 Hz to 50.1 Hz is added to prevent the inertia controller from acting at minor frequency deviations. Whether or not this dead band is realistic or optimal, and if a smaller or larger dead band should have been used was not in scope of this analysis. The constants K_{f1} and K_{f2} can be modified to change the response during a change in frequency. Further work on this thesis could involve an analysis of the tuning of these parameters for a more optimal response. Below are the speed references and power outputs for a frequency drop event for different combinations of K_{f1} and K_{f2}. The external grid is the same as in Scenario B where a 8kW load is connected at t = 20 seconds.

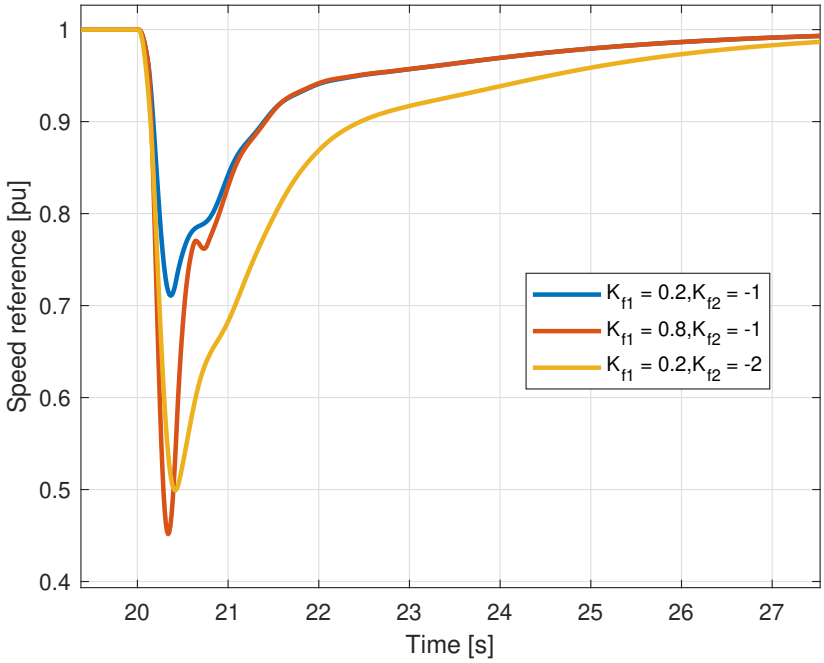

Figure 8.26: Speed reference for different combinations of K_{f1} and K_{f2}.

Of the presented combinations, $K_{f1} = 0.2$ and $K_{f2} = -2$ seems to give the smoothest response from the system, meaning no sharp power swings or oscillations in frequency. This ratio between the constants are used for further simulations, but their magnitude is reduced such that the speed reference does not decrease below 0.85 pu. The final combinations of K_{f1} and K_{f2} are given in Section 5.3.

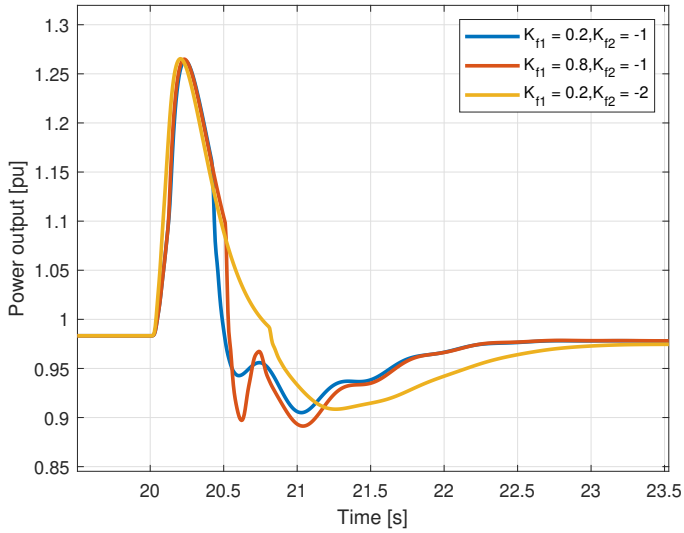

Figure 8.27: Power output for different combinations of K_{f1} and K_{f2}.

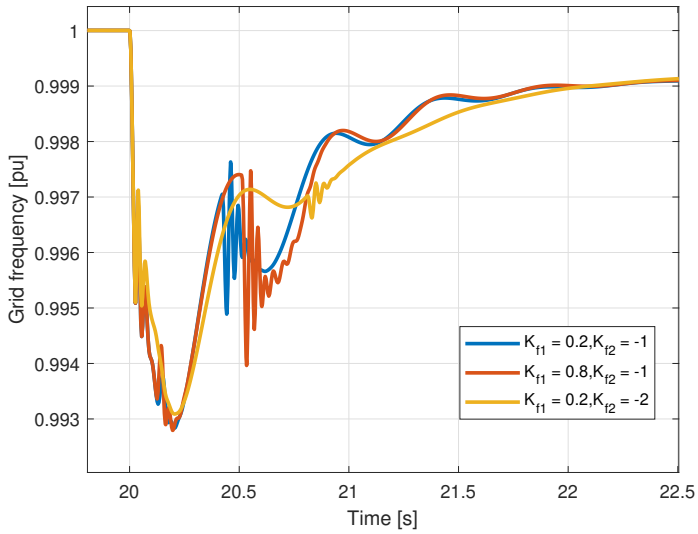

Figure 8.28: Frequency for different combinations of K_{f1} and K_{f2}.

E.1 Rotor Inertia Controller Implementation

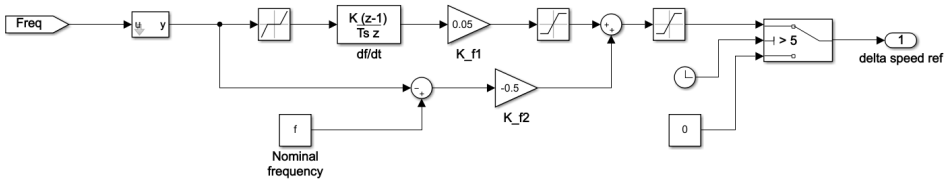

Figure 8.29: Rotor inertia controller.

F DC-link Capacitor Inertia Controller

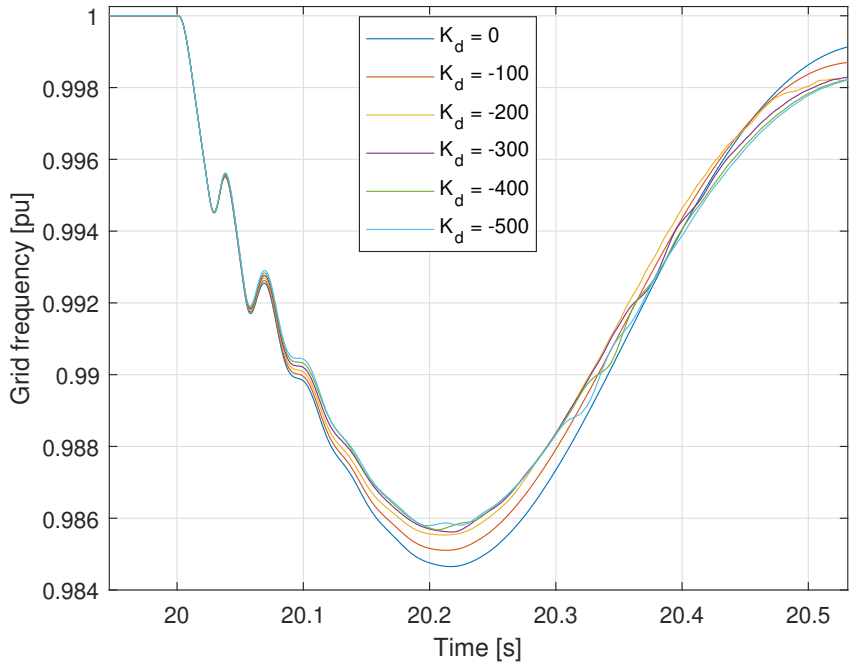

Figure 8.30: Initial frequency drop for different droop constants.

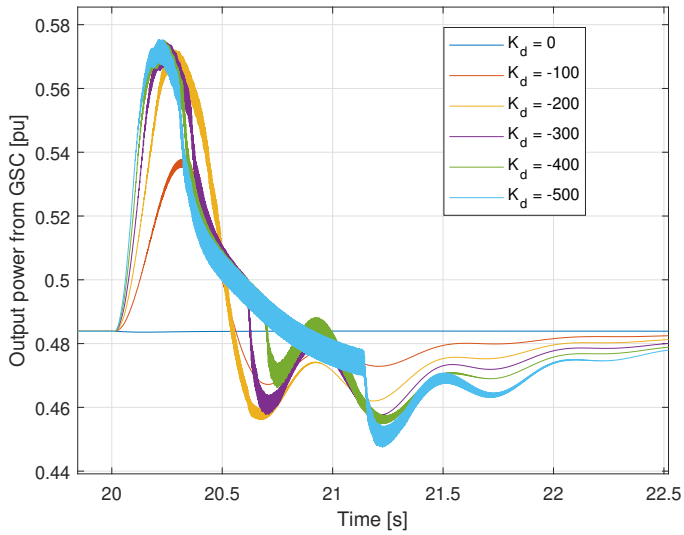

Figure 8.31: Power output from grid-side converter for different droop constants.

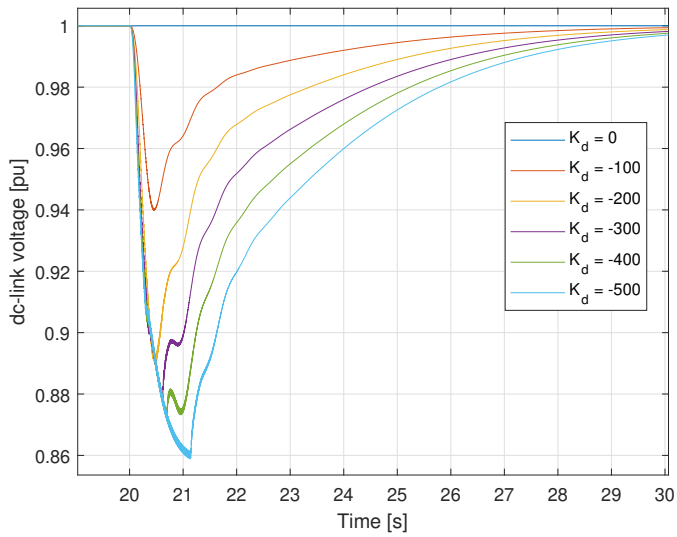

Figure 8.32: DC-link voltage for different droop constants.

F.1 DC-link Capacitor Inertia Controller Implementation

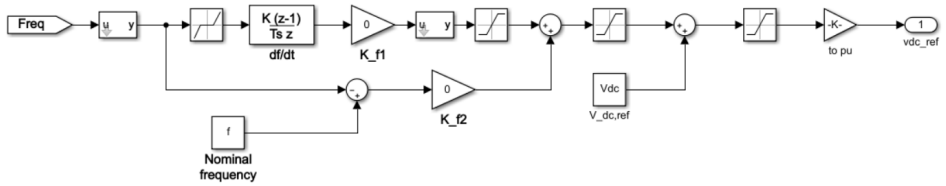

Figure 8.33: Capacitor inertia controller.

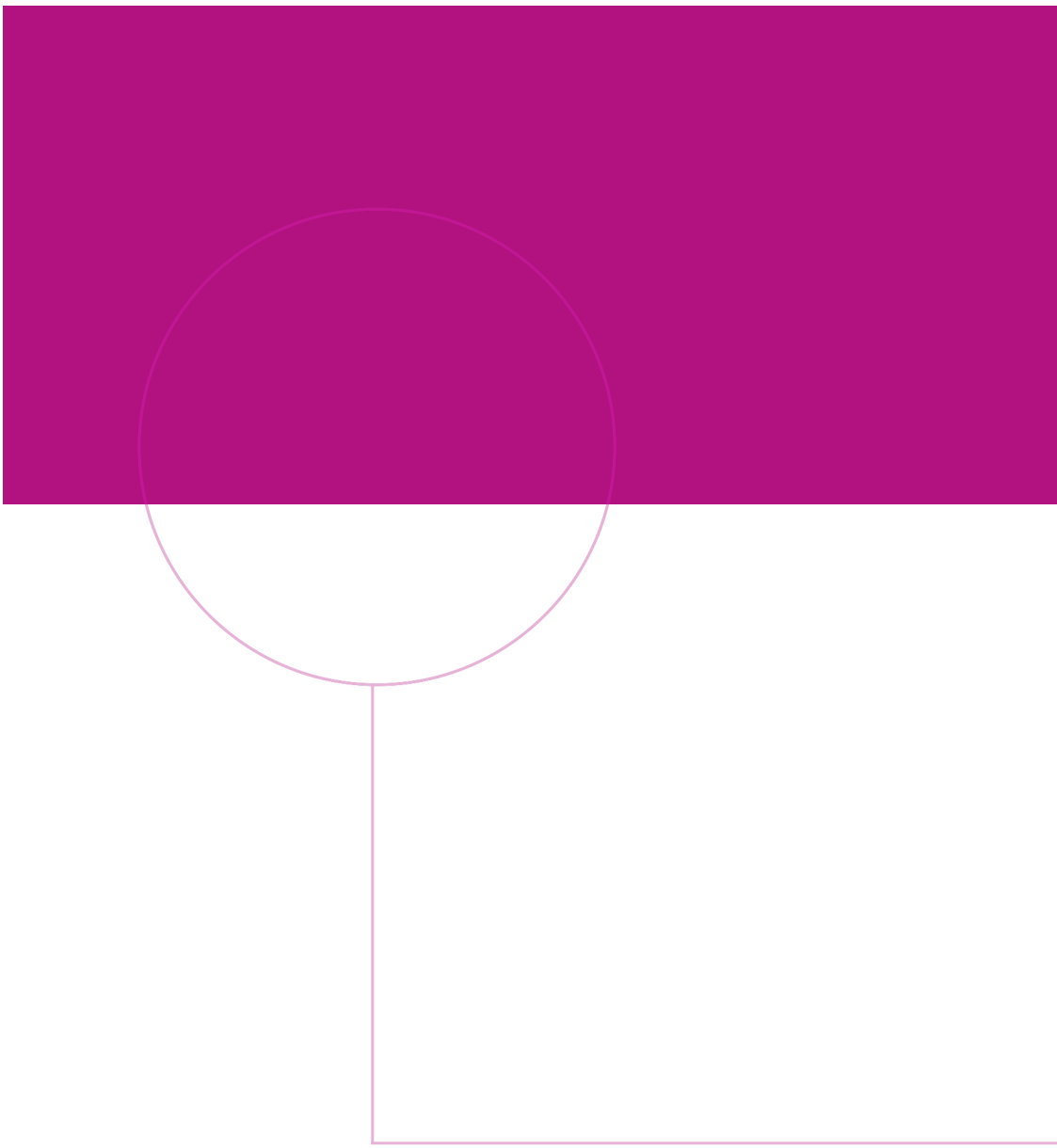

NTNU

Norwegian University of
Science and Technology